Eur. Phys. J. C (2025) 85:445
https://doi.org/10.1140/epjc/s10052-025-14055-7

THE EUROPEAN PHYSICAL JOURNAL C

Regular Article - Theoretical Physics

Axial-vector and scalar contributions to hadronic light-by-light scattering

Gernot Eichmann[1,a], **Christian S. Fischer**[2,3,b], **Tim Haeuser**[2], **Oliver Regenfelder**[1]

[1] Institute of Physics, University of Graz, NAWI Graz, Universitätsplatz 5, 8010 Graz, Austria
[2] Institut für Theoretische Physik, Justus-Liebig-Universität Gießen, 35392 Giessen, Germany
[3] Helmholtz Forschungsakademie Hessen für FAIR (HFHF), GSI Helmholtzzentrum für Schwerionenforschung, Campus Gießen, 35392 Giessen, Germany

Received: 13 November 2024 / Accepted: 9 March 2025

Abstract We present results for single axial-vector and scalar meson pole contributions to the hadronic light-by-light scattering (HLbL) part of the muon's anomalous magnetic moment. In the dispersive approach to these quantities (in narrow width approximation) the central inputs are the corresponding space-like electromagnetic transition form factors. We determine these directly using a functional approach to QCD by Dyson–Schwinger and Bethe–Salpeter equations in the very same setup we used previously to determine pseudo-scalar meson exchange (π, η and η') as well as meson (π and K) box contributions. Particular care is taken to preserve gauge invariance and to comply with short distance constraints in both the form factors and the HLbL tensor. Our result for the contributions from a tower of axial-vector states including short distance constraints is $a_\mu^{\text{HLbL}}[\text{AV-tower+SDC}] = 24.8\,(6.1) \times 10^{-11}$. For the combined contributions from $f_0(980)$, $a_0(980)$, $f_0(1370)$ and $a_0(1450)$ we find $a_\mu^{\text{HLbL}}[\text{scalar}] = -1.6\,(5) \times 10^{-11}$.

1 Introduction

The anomalous magnetic moment $a_\mu = \frac{1}{2}(g-2)_\mu$ of the muon is under intense scrutiny from both theory and experiment. With updated results from 2019 and 2020 data runs of the Fermilab muon $g-2$ experiment, the experimental world average $a_\mu(\text{exp}) = 116\,592\,059\,(22) \times 10^{-11}$ [1] has an uncertainty reduced by more than a factor of two compared to the earlier BNL experiment [2,3]. The theoretical error of the Standard Model prediction of this quantity [4–31] is dominated by the error in the hadronic contributions, i.e. the hadronic vacuum polarisation (HVP) and hadronic light-by-light scattering (HLbL) displayed in Fig. 1. In order to reduce this theoretical error it is mandatory to improve both. The size of the HLbL contribution to a_μ has been estimated in a White Paper of the Muon $g-2$ Theory Initiative, $a_\mu(\text{HLbL}) = 92\,(19) \times 10^{-11}$ [4,17,21–29,32–37], with an error budget dominated by uncertainties in the contributions from axial-vector meson poles and short-distance physics. Contributions from scalar mesons beyond the leading s-wave rescattering effects also have large uncertainties but are considered to be much smaller in size. In this work we focus on contributions from intermediate meson states with both axial-vector and scalar quantum numbers with the goal to contribute to reducing these uncertainties.

While leading pole contributions with pseudoscalar quantum numbers (π_0, η, η') are well under control [20,21,24–26,38–44], subleading contributions from axial-vectors are still under much scrutiny. Technical issues such as the problem of kinematic singularities in the basis of the HLbL tensor have been addressed in Ref. [45], leading to an optimised basis which we will utilize in this work. Progress has also been made in identifying necessary ingredients for satisfying short-distance constraints (SDC) [27,46–48]. These were identified by Melnikov and Vainshtein [17] and have subsequently led to intense debates on the detailed mechanism of their realisation in terms of the axial anomaly, single- and double off-shell pseudoscalar and axial-vector transition form factors (axTFF), and contributions from infinite towers of pseudoscalar and axial-vector states. Recent discussions on this issue can be found in [28,29,49–58].

Another technical complication in the determination of the transition form factors (TFFs) of the axial-vector (AV) and scalar (S) states is gauge invariance. The general tensor

[a] e-mail: gernot.eichmann@uni-graz.at
[b] e-mail: christian.fischer@theo.physik.uni-giessen.de (corresponding author)

Published online: 22 April 2025

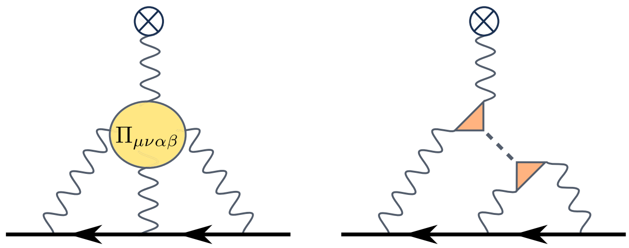

Fig. 1 Left: HLbL scattering contribution to a_μ. The main ingredient is the hadronic photon four-point function $\Pi_{\mu\nu\alpha\beta}$. Right: Meson-exchange part of the HLbL contribution to a_μ (without permutations of the photon legs)

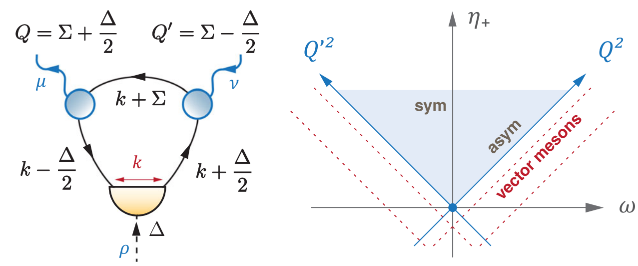

Fig. 2 Left: Meson $\rightarrow$ $\gamma^{(*)}\gamma^{(*)}$ transition matrix element. Right: Kinematic domains in Q^2 and Q'^2 including the symmetric and asymmetric limits; the dotted lines show the vector-meson pole locations

decomposition of the corresponding current leads to six (AV) and five (S) different tensor structures, which reduce to five each due to transversality of the axial-vector meson. Furthermore, the corresponding form factors of two (AV) and three (S) structures must vanish due to gauge invariance. The latter constraint is easily overlooked in quark model calculations but is vital to guarantee the absence of model artefacts in the remaining physical form factors.

In this work we employ a microscopic approach to QCD that satisfies both small and large momentum constraints on the TFFs as well as constraints due to gauge invariance. We work with a rainbow-ladder truncation of the Dyson–Schwinger and Bethe–Salpeter equations (DSEs and BSEs) of QCD that has delivered results for the pseudoscalar pion, η and η' pole contributions to HLbL [41,59,60] in very good agreement with the data-driven dispersive approach as well as lattice QCD.[1] The same is true for the pion box contribution [41]. Furthermore, our prediction for the kaon box contribution [36] has later been confirmed by the dispersive approach [62].

In the next Sect. 2 we detail our calculations for the axial-vector and scalar transition form factors and discuss our results. In Sect. 3 we present corresponding results for HLbL and we conclude in Sect. 4. We use a Euclidean notation throughout this work; see e.g. Appendix A of Ref. [63] for conventions.

2 Transition form factors

2.1 Matrix elements

We consider the axial-vector two-photon transition matrix element $\Lambda_A^{\mu\nu\rho}(Q,Q')$ and its scalar counterpart $\Lambda_S^{\mu\nu}(Q,Q')$, which we collectively denote by $\Lambda_{\mathrm{M}}^{\mu\nu(\rho)}(Q,Q')$ with $\mathrm{M} = A, S$. Our conventions are shown in Fig. 2: Q' and Q are the incoming and outgoing photon four-momenta, respectively. They can be expressed through the average photon momentum $\Sigma = (Q+Q')/2$ and the incoming meson momentum $\Delta = Q - Q'$, which is onshell ($\Delta^2 = -m_{\mathrm{M}}^2$). The process then depends on two Lorentz invariants, either Q^2 and Q'^2 or their linear combinations

$$\eta_+ = \frac{Q^2+Q'^2}{2}, \quad \omega = \frac{Q^2-Q'^2}{2}, \tag{1}$$

while the third variable is fixed by the onshell constraint:

$$\eta_- = Q\cdot Q' = \frac{Q^2+Q'^2+m_M^2}{2}. \tag{2}$$

The amplitude is Bose-symmetric,

$$\Lambda_{\mathrm{M}}^{\mu\nu(\rho)}(Q,Q') = \Lambda_{\mathrm{M}}^{\nu\mu(\rho)}(-Q',-Q), \tag{3}$$

and electromagnetic gauge invariance implies transversality in the photon legs:

$$Q^\mu \Lambda_{\mathrm{M}}^{\mu\nu(\rho)}(Q,Q') = 0, \qquad Q'^\nu \Lambda_{\mathrm{M}}^{\mu\nu(\rho)}(Q,Q') = 0. \tag{4}$$

In App. A we show that the most general tensor decomposition of the axial-vector matrix element that implements Bose symmetry and is free of kinematic constraints can be written as

$$\Lambda_A^{\mu\nu\rho}(Q,Q') = m_A \sum_{i=1}^{6} F_i^A(Q^2,Q'^2)\,\tau_i^{\mu\nu\rho}(Q,Q'), \tag{5}$$

with six dimensionless form factors F_i^A and corresponding dimensionless Lorentz tensors τ_i:

$$\begin{aligned}
m_A^3\,\tau_1^{\mu\nu\rho} &= \frac{1}{2}\left(\varepsilon_Q^{\mu\rho\alpha}\,t_{Q'Q'}^{\alpha\nu} - t_{QQ}^{\mu\alpha}\,\varepsilon_{Q'}^{\nu\rho\alpha}\right),\\
m_A^5\,\tau_2^{\mu\nu\rho} &= \frac{\omega}{2}\left(\varepsilon_Q^{\mu\rho\alpha}\,t_{Q'Q'}^{\alpha\nu} + t_{QQ}^{\mu\alpha}\,\varepsilon_{Q'}^{\nu\rho\alpha}\right),\\
m_A^5\,\tau_3^{\mu\nu\rho} &= 2\omega\,\varepsilon_{QQ'}^{\mu\nu}\,\Sigma^\rho,\\
m_A^3\,\tau_4^{\mu\nu\rho} &= \varepsilon_{QQ'}^{\mu\nu}\,\Delta^\rho,\\
m_A\,\tau_5^{\mu\nu\rho} &= \varepsilon_\Sigma^{\mu\nu\rho},\\
m_A^3\,\tau_6^{\mu\nu\rho} &= \omega\,\varepsilon_\Delta^{\mu\nu\rho}.
\end{aligned} \tag{6}$$

[1] Our framework also delivers results for the HVP contribution in the ballpark of dispersive and lattice results, although the error of roughly 3% is much too large to make any claims for this quantity [61].

Here and in the following we abbreviate

$$
\begin{aligned}
\varepsilon_a^{\mu\alpha\beta} &= \varepsilon^{\mu\alpha\beta\lambda} a^\lambda, \\
\varepsilon_{ab}^{\mu\nu} &= \varepsilon^{\mu\nu\alpha\beta} a^\alpha b^\beta, \\
t_a^{\mu\alpha\beta} &= \delta^{\mu\beta} a^\alpha - \delta^{\mu\alpha} a^\beta, \\
t_{ab}^{\mu\nu} &= a\cdot b\, \delta^{\mu\nu} - b^\mu a^\nu,
\end{aligned} \tag{7}
$$

where a and b are four-momenta. Electromagnetic gauge invariance eliminates the tensors τ_5 and τ_6, which entails that F_5^A and F_6^A must vanish. Our calculation satisfies this requirement as long as all ingredients entering in the matrix element are calculated consistently from the quark level; however, as discussed in App. B this is not automatic if one employs model inputs. From $a^\mu\, t_{ab}^{\mu\nu} = 0$ and $t_{ab}^{\mu\nu}\, b^\nu = 0$ the transversality of the remaining tensors $\tau_1 \dots \tau_4$ is manifest. Finally, the transversality of the axial-vector meson also eliminates τ_4 (see App. A).

The F_i^A are Bose-symmetric and therefore even in the variable ω, so they can be written as $F_i^A(\eta_+, \omega^2)$. Their kinematic region is shown in the right panel of Fig. 2: The two asymmetric (singly-virtual) limits correspond to $\omega = \pm\eta_+$ and the symmetric (doubly-virtual) limit implies $\omega = 0$. In the timelike region, the form factors must have vector-meson poles. Our form factors are related to the three form factors $\mathcal{F}_\mathrm{s}$, $\mathcal{F}_{\mathrm{a}_1}$ and $\mathcal{F}_{\mathrm{a}_2}$ in Refs. [57,64] by

$$
F_1^A = \mathcal{F}_\mathrm{s}, \quad F_2^A = -\frac{m_A^2}{\omega}\,\mathcal{F}_{\mathrm{a}_2}, \quad F_3^A = -\frac{m_A^2}{\omega}\,\mathcal{F}_{\mathrm{a}_1}. \tag{8}
$$

The analogous decomposition for the scalar matrix element is given by

$$
\Lambda_S^{\mu\nu}(Q, Q') = m_S \sum_{i=1}^{5} F_i^S(Q^2, Q'^2)\, \tau_i^{\mu\nu}(Q, Q') \tag{9}
$$

with

$$
\begin{aligned}
m_S^2\, \tau_1^{\mu\nu} &= -t_{QQ'}^{\mu\nu}, \\
m_S^4\, \tau_2^{\mu\nu} &= t_{QQ}^{\mu\alpha}\, t_{Q'Q'}^{\alpha\nu} \\
\tau_3^{\mu\nu} &= \delta^{\mu\nu}, \\
m_S^2\, \tau_4^{\mu\nu} &= Q^\mu Q'^\nu, \\
m_S^2\, \tau_5^{\mu\nu} &= Q^\mu Q^\nu + Q'^\mu Q'^\nu.
\end{aligned} \tag{10}
$$

In this case electromagnetic gauge invariance eliminates all tensors except τ_1 and τ_2, which leaves two dimensionless form factors $F_{1,2}^S(\eta_+, \omega^2)$.

2.2 Microscopic calculation

As in our previous works for the pseudoscalar transition form factors [41,59,60], we employ a rainbow-ladder truncation whose details can be found in Refs. [63,65]. For the convenience of the reader we also provide all explicit equations with short explanations in App. C.

The microscopic decomposition of the matrix element is then given by (see Fig. 2)

$$
\begin{aligned}
\Lambda_\mathrm{M}^{\mu\nu(\rho)} = 2\, c_M\, \mathrm{Tr} \int \frac{d^4k}{(2\pi)^4}\, S(k_+)\, \Gamma_\mathrm{M}^{(\rho)}(k, \Delta)\, S(k_-) \\
\times \Gamma^\mu(k_-, k+\Sigma)\, S(k+\Sigma)\, \Gamma^\nu(k+\Sigma, k_+).
\end{aligned} \tag{11}
$$

Here, $k_\pm = k \pm \Delta/2$ are the quark momenta. S denotes the fully dressed quark propagator, $\Gamma_\mathrm{M}^{(\rho)}$ the Bethe–Salpeter amplitude of the scalar and axial-vector meson, respectively, and Γ^μ is the fully dressed quark-photon vertex. The factor 2 in front comes from the symmetrization of the photon legs, which yields two identical diagrams, and c_M is the colour-flavour trace. The rainbow-ladder truncation induces ideal mixing and thus the a_1 and f_1 are mass degenerate whereas the f_1' is a pure $s\bar{s}$ state. Because our meson Bethe–Salpeter amplitudes are normalised to 1 in colour and flavour space, the colour trace is $\sqrt{3}$ and the combined colour-flavour factors are

$$
c_{a_{0,1}} = \frac{1}{\sqrt{6}}, \quad c_{f_{0,1}} = \frac{5}{3\sqrt{6}}, \quad c_{f'_{0,1}} = \frac{1}{3\sqrt{3}}. \tag{12}
$$

Note that on the r.h.s. of Eqs. (5) and (11) we suppressed the squared electric charge e^2 for brevity.

Equation (11) depends on several nonperturbative ingredients, which we determine from numerical solutions of their DSEs and BSEs. The renormalised dressed quark propagator $S^{-1}(p) = Z_f(p^2)\,(i\not{p} + M(p^2))$ involves the wave function $Z_f(p^2)$ and the quark mass function $M(p^2)$, which encodes effects of dynamical mass generation due to the dynamical breaking of chiral symmetry. The quark-photon vertex Γ^μ can be decomposed into twelve tensors; see e.g. App. B of Ref. [63] for details. Our numerical solution for the vertex from the inhomogeneous Bethe–Salpeter equation [65–69] dynamically generates timelike vector-meson poles in its transverse part, so the underlying physics of vector-meson dominance is already contained in the form factors without the need for further adjustments. Finally, the meson amplitudes $\Gamma_\mathrm{M}^{(\rho)}$ are determined from their homogeneous BSEs, see App. C.

In a rainbow-ladder calculation the masses of ground state pseudoscalar and vector mesons come out close to the experimental ones, whereas the axial-vector and scalar meson masses are quite far away: $m_A = 0.91$ GeV for a_1/f_1 and $m_S = 0.67$ GeV for a_0/f_0. Indeed, corrections beyond rainbow-ladder are needed to achieve agreement with experiment [70,71], and four-body calculations indicate that the $f_0(500)$ is predominantly a four-quark state with only a small $q\bar{q}$ component [72–74].

This mass discrepancy has a direct influence on the transition form factors via the various factors of m_A and m_S showing up in the matrix elements discussed above. We quote in the following the form factors $F_i^{A,S}$ obtained by multiplying the rainbow-ladder results $(F_i^{A,S})^\mathrm{RL}$ with powers of

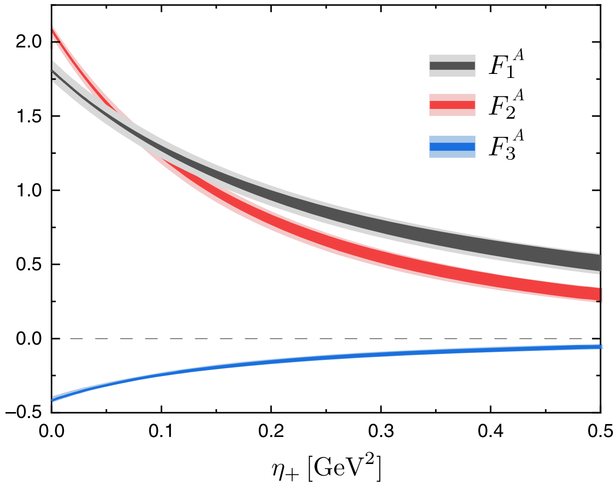

Fig. 3 Axial-vector transition form factors as functions of the average photon momentum $\eta_+ = (Q^2 + Q'^2)/2$. The darker bands cover the kinematic domain between the symmetric and asymmetric limits. The lighter bands include also the dependence on the shape parameter in the effective interaction

$(m_M^{\exp}/m_M^{\mathrm{RL}})$ according to

$$\sum_i (F_i^{A,S})\,\tau_i = \sum_i (F_i^{A,S})^{\mathrm{RL}}\,\tau_i^{\mathrm{RL}}. \tag{13}$$

Here, the τ_i are the tensors in Eqs. (6) and (10) with the experimental a_1 and a_0 masses, $m_A^{\exp} = 1.23$ GeV and $m_S^{\exp} = 0.98$ GeV, and the τ_i^{RL} are those using the rainbow-ladder masses m_A, m_S. These results are presented and discussed in Sects. 2.3 and 2.4. It turns out that the axialvector TFFs treated in this way lead to an acceptable value for the equivalent two-photon decay width of the $f_1(1285)$, whereas the scalar two-photon decay widths are not well represented. In order to treat all TFFs on the same footing, and to account for experimental constraints, we therefore choose a 'data-driven' approach by using the known experimental two-photon decay widths of the $f_1(1285)$ and the $f_0(980)$, $a_0(980)$, $f_0(1370)$ and $a_0(1450)$ as inputs for the normalisation of the TFFs, which are then employed in our calculations of the a_μ contributions in Sect. 3 below.

2.3 Axial-vector transition form factors

Our results for the three axial-vector transition form factors $F_i^A(Q^2, Q'^2)$ with $i = 1, 2, 3$ are shown in Fig. 3. The plotted curves correspond to the total contributions summing over the a_1, f_1 and f_1' via Eq. (12) under the assumption that their individual form factors are identical. The plot covers the full kinematic domain between the symmetric and asymmetric limits (dark bands). As in the case of the pion transition form factor [59,60], the angular dependence is very small and collapses into a narrow band in the average photon momentum η_+.

The authors of Refs. [57,75] provide parameterisations for the three form factors based on various experimental reactions involving the $f_1(1285)$, namely $e^+e^- \to e^+e^- f_1$, $e^+e^- \to f_1\pi^+\pi^-$ and the radiative decays $f_1 \to \rho\gamma$ and $f_1 \to \phi\gamma$. Expressed in terms of our F_i^A using Eq. (8), and summing again over the a_1, f_1 and f_1', in the limit $Q^2 = Q'^2 = 0$ this yields the constraints[2]

$$\begin{bmatrix} 2.45\,(35) \\ 1.96\,(42) \end{bmatrix}, \quad \begin{bmatrix} 2.18\,(1.17) \\ 0.42\,(1.49) \end{bmatrix}, \quad \begin{bmatrix} -0.74\,(84) \\ -0.33\,(84) \end{bmatrix} \tag{14}$$

for F_1^A, F_2^A and F_3^A, respectively, where the lower values include an additional constraint from $f_1 \to \phi\gamma$.

Figure 3 shows that our form factors are compatible with these values: F_1^A and F_2^A are large and positive while F_3^A is smaller and negative. Our results at $Q^2 = Q'^2 = 0$ are

$$F_1^A = 1.80\,(7), \quad F_2^A = 2.08\,(5), \quad F_3^A = -0.41\,(1), \tag{15}$$

where the errors come from a variation of the shape parameter $\eta = 1.8 \pm 0.2$ in the effective quark-gluon interaction. The corresponding errors at non-zero momenta Q^2, Q'^2 are visible in Fig. 3 as light coloured bands. These correspond to similar error bands as in our results of Ref. [41] for the pseudoscalar TFFs.

The form factor F_1^A is related to the equivalent two-photon decay width

$$\Gamma_{\gamma\gamma} = \frac{\pi\alpha^2}{48}\, m_A |F_1^A(0,0)|^2, \tag{16}$$

whose experimental value for the $f_1(1285)$ measured by the L3 collaboration is $\Gamma_{\gamma\gamma} = 3.5(6)(5)$ keV [76]. According to Eq. (12), our f_1 form factors are given by those in Eq. (15) multiplied with $c_{f_1}/(c_{a_1} + c_{f_1} + c_{f_1'})$, which yields $\Gamma_{\gamma\gamma} = 3.9(3)$ keV.

We should emphasize that the internal consistency of our calculations is crucial for the quality of our results. If any of the three ingredients (meson Bethe–Salpeter amplitude, quark propagator, quark-photon vertex) is replaced with model input, the magnitudes and shapes of the form factors can change substantially and F_2^A and F_3^A can even switch signs, see Fig. 6 in App. B. In addition, with model inputs also electromagnetic gauge invariance is not automatic and the form factors F_5^A and F_6^A are non-zero and sizeable, even if the electromagnetic Ward–Takahashi identity (WTI) that relates the quark propagator and quark-photon vertex is intact. The rainbow-ladder truncation, on the other hand, satisfies the WTI already at the level of the BSE kernel and thereby automatically ensures the consistency of all ingredients and the electromagnetic gauge invariance of the matrix elements. A detailed discussion of this issue can be found in App. B.

[2] To be compatible with our conventions with positive flavour factors, we switched the sign of the f_1' contribution in Ref. [57] since the authors employ a minus sign in their flavour basis.

In practice, a robust extraction of the form factors for large values of η_+ is currently limited to $\eta_+ \lesssim 150\ \text{GeV}^2$ near the symmetric limit $|\omega|/\eta_+ \ll 1$. For larger values of $|\omega|/\eta_+$ one would need contour deformations to deal with the singularities in the integrand [60]. For larger values of η_+, the results for F_2^A and F_3^A are numerically too noisy because their respective tensors vanish in the symmetric limit. For large η_+ also the angular dependence of the quark-photon vertex dressing functions (which we neglect here) becomes relevant since in the symmetric limit the vertex is tested in kinematics where one quark is soft and the other hard. This would require a moving-frame solution of the quark-photon vertex BSE which is beyond the scope of the present work.

In the following we provide parametrizations of the numerical data of our form factors for further use in the HLbL amplitude. Although for the muon $g-2$ calculation only their behavior at low $Q^2 \ll 10\ \text{GeV}^2$ is relevant, here we also attempt to implement their large $Q^2 \gg 100\ \text{GeV}^2$ behavior. A light-cone expansion entails the following asymptotic behavior for $\eta_+ \to \infty$ [64]:

$$F_1^A \to \frac{f_{\text{eff}}^A m_A^3}{\eta_+^2}\, h_1(w), \quad F_2^A \to \frac{2 f_{\text{eff}}^A m_A^5}{5\,\eta_+^3}\, h_2(w), \tag{17}$$

with $w = \omega/\eta_+$ and

$$h_1(w) = -\frac{3}{w^2}\left(1 + \frac{1}{2w}\ln\frac{1-w}{1+w}\right),$$
$$h_2(w) = -\frac{15}{8w^4}\left(6 + \frac{3-w^2}{w}\ln\frac{1-w}{1+w}\right). \tag{18}$$

In the symmetric limit this implies $h_1(0) = h_2(0) = 1$, whereas in the asymmetric limits the h_i diverge logarithmically. The remaining form factor behaves like $F_3^A \sim 1/\eta_+^3$ for large η_+. The effective decay constant f_{eff}^A in Eq. (17) sums over the a_1, f_1 and f_1'. Assuming that all three states have the same decay constant f_A, then for ideal mixing one obtains

$$f_{\text{eff}}^A \approx \frac{4}{\sqrt{6}}\,(c_{a_1} + c_{f_1} + c_{f_1'})\, f_A. \tag{19}$$

In the accessible η_+ range near the symmetric limit we see the onset of the asymptotic scaling behavior $F_1^A \sim 1/\eta_+^2$ and $F_2^A \sim 1/\eta_+^3$. F_3^A, on the other hand, develops a zero crossing around $\eta_+ \approx 30\ \text{GeV}^2$ and remains positive for large η_+.

To match with the asymptotic constraints away from the symmetric limit, we parametrize our form factors for $x \geq 0$ and $|w| < 1$ as follows:

$$F_i^A(x, w) = G_i^A(x)\, H_i^A(x, w) \tag{20}$$

Table 1 Fit parameters for our axial-vector transition form factors $F_i^A(x, w)$

i	a_i	b_i	c_i	d_i	e_i	ν_i	μ_i	λ_i
1	1.80 (7)	3.28	4.64 (50)	4.74	24.9	2	1.6	4.0
2	2.08 (5)	6.45	4.74 (23)	8.22	11.7	3	1.6	5.0
3	−0.41(1)	−1.31	1.22 (23)	−56.0	64.4	3	–	–

with $x = \eta_+/m_\rho^2$, $m_\rho = 0.77$ GeV, and

$$G_i^A(x) = \frac{1}{(1+x)^{2\nu_i}}\left(a_i + b_i\,x + c_i\,x^{\nu_i}\,\frac{x+d_i}{x+e_i}\right),$$
$$H_1^A(x, w) = 1 + \sum_{n=1}^{N}\frac{x^{\mu_1}}{x^{\mu_1} + \lambda_1 n}\,\frac{w^{2n}}{1+\frac{2n}{3}},$$
$$H_2^A(x, w) = 1 + \sum_{n=1}^{N}\frac{x^{\mu_2}}{x^{\mu_2} + \lambda_2 n}\,\frac{(1+n)\,w^{2n}}{\left(1+\frac{2n}{3}\right)\left(1+\frac{2n}{5}\right)},$$
$$H_3^A(x, w) = 1. \tag{21}$$

Because of $H_i^A(x, 0) = 1$ the form factors in the symmetric limit reduce to the $G_i^A(x)$, whose parameters are listed in Table 1. From the series expansion of the logarithms in Eq. (18) one obtains

$$h_1(w) = 1 + \sum_{n=1}^{\infty}\frac{w^{2n}}{1+\frac{2n}{3}},$$
$$h_2(w) = 1 + \sum_{n=1}^{\infty}\frac{(1+n)\,w^{2n}}{\left(1+\frac{2n}{3}\right)\left(1+\frac{2n}{5}\right)}, \tag{22}$$

which entails that $H_i^A(x \to \infty, w) = h_i(w)$ for $N \to \infty$. Therefore, the functions $H_i^A(x, w)$ interpolate between $H_i^A(x = 0, w) = 1$ and $H_i^A(x \to \infty, w) = h_i(w)$. In the absence of asymptotic constraints for F_3^A we set $H_3^A(x, w) = 1$.

Note that the fit parameters a_i and c_i control the magnitude of the form factors at small and large x, respectively. We absorbed the dependence on the shape parameter in the effective interaction, which is a measure of our systematic uncertainty, in the errors of the a_i and c_i which are shown by the lighter bands in Fig. 3. All other errors in the fitting procedure are completely negligible compared to this systematic error and are consequently not taken into account in our error budget. Note also that the powers ν_i are integer only and the fixed mass scale m_ρ in Eq. (21) is not varied while fitting.

The quality of our parametrisations may be inferred from the comparison in Appendix D; the numerical results and fits are indistinguishable by eye. We note that the convergence behaviour of the sums in Eq. (21) is rather slow. We used $N = 100$ terms to obtain good fits with sub-permille accuracy in the region of low η_+ shown in Fig. 3, where

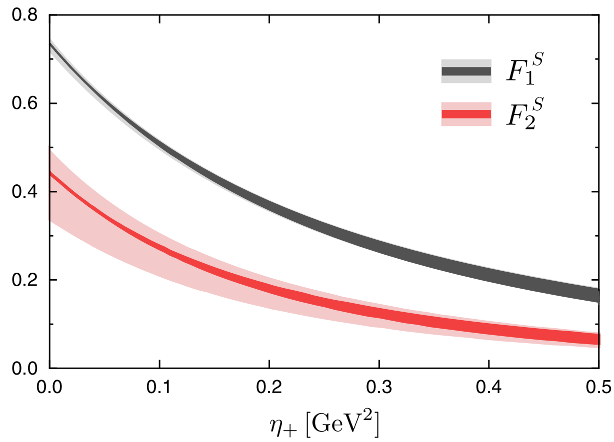

Fig. 4 Scalar transition form factors as functions of η_+, see Fig. 3 for details

the singly-virtual case is directly calculable. For larger η_+ this number would need to further increase to reproduce the asymptotic logarithms via the series expansion. Note also that we do not attempt to provide a realistic parametrization for timelike values in terms of vector-meson poles, although in principle this could also be achieved using a series representation. For the calculation of a_μ, we increased N until our numerical results for the various contributions to a_μ did not change on the sub-permille level. This goal was achieved for $N \approx 60$ and we then did all calculations with $N = 100$ to be on the safe side.

2.4 Scalar transition form factors

The analogous results for the scalar transition form factors obtained from Eq. (11), $F_i^S(Q^2, Q'^2)$ with $i = 1, 2$, are displayed in Fig. 4. Like in the axial-vector case, we sum up the three light flavour states a_0, f_0 and f_0' whose colour-flavour factors are given by Eq. (12). Also in this case the angular dependence is small and yields a narrow band in η_+ (dark bands). The light coloured bands correspond again to the variation of the shape parameter in the effective quark-gluon interaction.

At asymptotically large values $\eta_+ \to \infty$, the two form factors behave as [64,77]

$$F_1^S \to \frac{3 f_{\text{eff}}^S m_S}{5\eta_+} h_0(w), \quad F_2^S \to \frac{3 f_{\text{eff}}^S m_S^3}{5\,\eta_+^2} h_0(w), \tag{23}$$

again with $w = \omega/\eta_+$ and

$$h_0(w) = \frac{5}{2w^4}\left(3 - 2w^2 + 3\,\frac{1-w^2}{2w}\ln\frac{1-w}{1+w}\right)$$
$$= 1 + \sum_{n=1}^{\infty} \frac{w^{2n}}{\left(1+\frac{2n}{3}\right)\left(1+\frac{2n}{5}\right)}. \tag{24}$$

Table 2 Fit parameters for our scalar transition form factors $F_i^S(x, w)$

i	a_i	b_i	c_i	d_i	e_i	ν_i	μ_i	λ_i
1	0.73 (2)	0	0.19 (2)	−15.3	14.9	1	1.6	2.6
2	0.41 (9)	0.46	0.37 (5)	−10.7	12.4	2	2.4	0.7

The effective decay constant f_{eff}^S is analogous to its axial-vector counterpart (19). We parametrize our form factors for $x \geq 0$ and $|w| < 1$ in the same way as before,

$$F_i^S(x, w) = G_i^S(x)\, H_i^S(x, w) \tag{25}$$

with $x = \eta_+/m_\rho^2$, $m_\rho = 0.77$ GeV, and

$$G_i^S(x) = \frac{1}{(1+x)^{2\nu_i}}\left(a_i + b_i\, x + c_i\, x^{\nu_i}\,\frac{x+d_i}{x+e_i}\right),$$
$$H_i^S(x, w) = 1 + \sum_{n=1}^{N} \frac{x^{\mu_i}}{x^{\mu_i} + \lambda_i n}\,\frac{w^{2n}}{\left(1+\frac{2n}{3}\right)\left(1+\frac{2n}{5}\right)} \tag{26}$$

for $i = 1, 2$. The fit parameters in this case are listed in Table 2. At low η_+, both form factors fall off considerably faster compared to their asymptotic powers and F_2^S even becomes negative at intermediate values of η_+. At large η_+ both form factors are positive and the asymptotic constraint $F_2^S/F_1^S \to m_S^2/\eta_+$ from Eq. (23) is reproduced.

Like in the axial-vector case, the consistency of our truncation is essential for these results. If any of the ingredients is replaced with models, electromagnetic gauge invariance is broken, the unphysical form factors $F_{3,4,5}^S$ in Eq. (9) are nonzero and the magnitudes and shapes of the physical form factors can differ substantially, as shown in Fig. 7 in App. B.

3 Axial-vector and scalar meson pole contributions to HLbL

We now proceed to discuss our results for the contribution of axial-vector and scalar states to HLbL in narrow width approximation. To this end we employ the formalism developed in Refs. [23,45]. Denoting the HLbL tensor by

$$\Pi^{\mu\nu\lambda\sigma} = \sum_{i=1}^{54} T_i^{\mu\nu\lambda\sigma}\, \Pi_i, \tag{27}$$

with scalar functions Π_i and Lorenz structures as in Ref. [23], the HLbL master formula reads

$$a_\mu^{\text{HLbL}} = \frac{\alpha^3}{432\pi^2}\int_0^\infty d\Sigma\,\Sigma^3 \int_0^1 dr\, r\sqrt{1-r^2}\int_0^{2\pi} d\phi$$
$$\times \sum_{i=1}^{12} T_i(\Sigma, r, \phi)\, \bar{\Pi}_i(q_1^2, q_2^2, q_3^2), \tag{28}$$

where the Euclidean momenta $Q_{1,2,3}^2 = -q_{1,2,3}^2$ are parametrized via [78]

$$
\begin{aligned}
Q_1^2 &= \frac{\Sigma}{3}\left(1 - \frac{r}{2}\cos\phi - \frac{r}{2}\sqrt{3}\sin\phi\right),\\
Q_2^2 &= \frac{\Sigma}{3}\left(1 - \frac{r}{2}\cos\phi + \frac{r}{2}\sqrt{3}\sin\phi\right),\\
Q_3^2 &= \frac{\Sigma}{3}\left(1 + r\cos\phi\right).
\end{aligned}
\tag{29}
$$

The kernel functions T_i are given in the appendix of Ref. [23]. The twelve scalar functions $\bar{\Pi}_i$ are generated by six representative scalar functions $\hat{\Pi}_i, i \in \{1, 4, 7, 17, 39, 54\}$ by explicit and crossing relations given in Eqs. (2.7) and (2.8) in Ref. [45]. For a given contribution, these depend explicitly on the transition form factors and propagators of the respective mesons as detailed below.

3.1 Axial-vector mesons: $J^{PC} = 1^{++}$

In Ref. [45] the six representative scalar functions for the case of axial-vector meson exchange are given in their Eq. (4.11), again with momenta $q_i^2 = -Q_i^2$ and the axial-vector transition form factors $\mathcal{F}_1^A, \mathcal{F}_2^A, \mathcal{F}_3^A$ written in a Minkowski basis which translates into our Euclidean one according to Eq. (8). These form factors are related to ours via

$$
\begin{aligned}
\mathcal{F}_1^A &= -\frac{\omega}{m_A^2}\, F_3^A,\\
\mathcal{F}_2^A &= \frac{1}{2}\left(F_1^A - \frac{\omega}{m_A^2}\, F_2^A\right),\\
\mathcal{F}_3^A &= -\frac{1}{2}\left(F_1^A + \frac{\omega}{m_A^2}\, F_2^A\right).
\end{aligned}
\tag{30}
$$

As already mentioned in the introduction, the important issue of short-distance constraints (SDCs) to the HLbL tensor is tightly connected to the anomaly and the role of axial-vector mesons. Detailed discussions can be found in the literature [28,29,49–51,53–58]. Within the framework of holographic QCD, it has been shown analytically that a resummation of contributions from an infinite tower of axial-vector states indeed serves to satisfy the SDCs [50,51,55,56]. The mechanism is quite interesting: while the asymptotic behaviour of each and every single axial-vector contribution to the HLbL tensor falls off too strongly with asymptotic momentum Q^2, the infinite resummation generates an extra power of Q^2 that leads to the correct asymptotics. This mechanism has been summarised and systematically compared to other suggested solutions in Ref. [54].

In our approach, we are not in a position to provide the same analytic proof. As already discussed, our TFFs automatically have the correct asymptotic large momentum behaviour, since perturbation theory is ingrained into the DSE framework. However, our TFFs are calculated not analytically but numerically with the difficulty that additional numerical problems appear at large momenta. As discussed above, advanced methods to handle these are available in principle but their implementation to the problem at hand requires much more work. This is relegated to the future, together with a more detailed study of the SDCs in our approach. For now we follow a more modest goal. We include not an infinite, but a sufficiently rich tower of axial-vector states such that their total contribution to a_μ saturates. In a second step we study the impact of SDCs using the matching prescription with the quark loop suggested in Refs. [29,54].

We perform the first of these tasks as follows. In Sect. 2.3 we found our TFFs to nicely match the experimental constraints, although the masses of our axial-vector states are too low. This motivates the assumption that the axTFFs do not change drastically throughout the whole tower of states. Thus we may use our result for the axTFFs of the ground state as proxy also for all other states. For the masses of the first two multiplets of a_1, f_1 and f_1' states we use the central values of the experimentally seen a_1 states, i.e. $m_{a_1(1260)} = 1230(40)$ MeV and $m_{a_1(1640)} = 1655$ MeV (Breit–Wigner masses) [79].[3] Since the experimental masses of the corresponding f_1 and f_1' states are larger, we therefore provide an upper bound for those contributions. In order to get a rough idea of the size of contributions from higher multiplets, we solved a simple Schrödinger equation for a quark model with Richardson type potential $V(r) = -\alpha/r + b\,r$ with constituent quarks of mass $M = 350$ MeV and matched the two parameters to the masses of the $a_1(1260)$ ($j = 1$) and $a_1(1640)$ ($j = 2$). This is achieved to good accuracy with $\alpha = 1.6$ and $b = 0.068$ GeV^2. The numerical results for the masses of the radial excitations with main quantum number $n = j + 1 > 3$ then follow the curve

$$
M^2(n) = (-0.76 + 1.095\,n + 0.016\,n^2)\,\text{GeV}^2, \tag{31}
$$

which is Regge-like for small n. We use these as masses for our tower of axial-vector multiplets.

Furthermore, as already indicated at the end of Sect. 2.2, we re-normalise our axialvector form factors using the two-photon decay width

$$
|F_1^A(0,0)|^2 = \frac{48\,\Gamma_{\gamma\gamma}}{\pi\alpha^2 m_A} \tag{32}
$$

[3] Assuming mass degeneracy within a given multiplet simplifies the calculation of its contribution to HLBL, since the corresponding flavour and charge factors can be summed analytically [50], which in our conventions from Eq. (12) amounts to a factor

$$
\frac{c_a^2 + c_f^2 + c_{f'}^2}{(c_a + c_f + c_{f'})^2} = \frac{2N_c \sum_a \left[\mathrm{tr}(t^a \mathcal{Q}^2)\right]^2}{(c_a + c_f + c_{f'})^2} = \frac{36}{(8+\sqrt{2})^2},
$$

with $\mathcal{Q} = \mathrm{diag}(2/3, -1/3, -1/3)$, $t^a = \lambda^a/2$, $t^0 = \mathbb{1}/\sqrt{6}$, Gell-Mann matrices λ^a, and the sum goes over $a = 0, 3, 8$.

Table 3 Results for a_μ^{AV} in units of 10^{-11}. Shown are integrated results for the ground-state multiplet ($j = 1$) as well as two, ten and twenty multiplets. In the second column we display fully integrated results and in the third column those integrated below a matching scale, see text for details

	Full	Matched
$j = 1$	17.4 (4.0)(4.0)(0.5)	
$j \leq 2$	20.9 (4.8)(4.3)(0.6)	
$j \leq 10$	23.6 (5.4)(4.4)(0.7)	
$j \leq 20$	23.8 (5.4)(4.4)(0.7)	24.8 (6.1) $\times 10^{-11}$

of the $f_1(1285)$ with $\Gamma_{\gamma\gamma} = 3.5(6)(5)$ keV, as measured by the L3 collaboration [76].

Our individual integrated results for the lowest-lying multiplets are displayed in the upper row of Table 3. In our calculation we observe that fifteen multiplets are enough to obtain a converged result on the level of 0.01×10^{-11}. To be on the safe side, we stopped after twenty multiplets, which is also our result for the whole infinite tower:

$$a_\mu^{\text{HLbL}}[\text{AV-tower}] = 23.8\,(5.4)(4.4)(0.7) \times 10^{-11}. \tag{33}$$

The first error propagates the uncertainty of the input value for the two-photon decay width to our final result. The second error reflects the model-related uncertainty due to the mismatch of the rainbow-ladder axialvector mass as compared to the experimental value: Whereas the global TFF is properly rescaled to match Eq. (32), the relative strength of F_1^A to $F_{2,3}^A$ is still affected by this mismatch. To take this into account, we determine the difference between using the (re-normalised) TFFs F_i^A obtained from the prescription in Eq. (13) and using the unnormalized $(F_i^A)^{\text{RL}}$ obtained with the rainbow-ladder axialvector mass in the tensor structures as a measure for the possible spread of results. The error reflecting this difference is about equal in magnitude to the one inflicted by the uncertainty of the experimental mass of the $a_1(1260)$. Both have been already added in quadrature. The third contribution to our error budget stems from the same variation of the model parameter η that leads to the light shaded bands in our TFFs, Fig. 3. Finally, the error introduced by using fits to our numerical results for the TFFs when calculating a_μ (cf. Appendix D) as well as the numerical error of the VEGAS routine used to perform the integrations for a_μ are both negligible by orders of magnitude and therefore not shown.

Our result, even when comparing on the level of single axial-vector pole contributions, is considerably larger than previous model results such as Refs. [32,34] and the White Paper estimate [4]. It is, however, of comparable size as results from holographic models [50,51,55,56,80]. Figure 5 shows a comparison of the axTFFs of our approach with the one of the HW2-model of Ref. [50]. Although there are

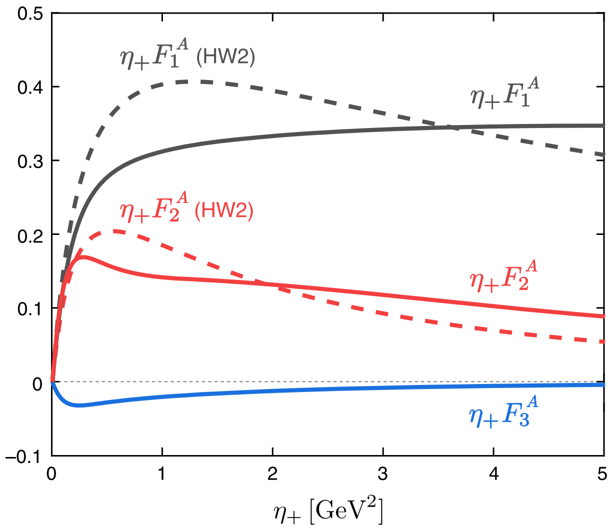

Fig. 5 Comparison of our axial-vector transition form factors in the asymmetric, i.e., singly-virtual limit (solid curves) with the corresponding ones from holographic QCD in the HW2 model [50] (dashed curves; $F_3^A = 0$ in their model). All values are in GeV^2

differences in the details of the momentum dependence, the overall orders of magnitude are similar.

We emphasise again that our framework satisfies constraints from gauge symmetry (cf. App. B), and our representations of the TFFs satisfy the SDCs on the level of the TFFs, Eqs. (17) and (18), by construction. To study the impact of the short distance constraints on the hadronic light-by-light tensor, we adopt the matching procedure with the perturbative quark loop suggested in Refs. [29,54]. The NLO corrections to the massless quark loop were determined recently in Ref. [47] and found to reduce the error associated with the quark loop contributions drastically. In Refs. [29,54] a tower of pseudoscalar meson pole contributions was matched to the quark loop results, but it was pointed out that the matching procedure is general and may as well be applied to a tower of axial-vector states. Since there are good arguments that this is anyhow what should be done [50,55], we adopt the procedure here as well. The general idea is to cut the integration of the tower of axial-vector states at a matching scale Q_{min} and add the mixed regions with two large and one small momentum by a suppression factor $Q_i^2/(Q_i^2 + Q_{\text{min}}^2)$ for the small momentum Q_i while retaining the cut that the two other momenta are larger than Q_{min}, see [29] for more details. For simplicity and comparability, we choose the same matching scale $Q_{\text{min}} = 1.7\,(5)$ GeV as in [29,54] and therefore obtain the same quark loop contribution $a_\mu^{\text{HLbL}}[\text{q-loop}(N_f = 3)] = 4.2\,(1) \times 10^{-11}$ as in Ref. [54]. The reduced contributions from the axial-vector states with this procedure can be found in the lower line of Table 3. It is quite satisfactory to see that the overall reduction of these contributions is of the same order as the quark-loop contributions. We therefore obtain as our final estimate

$$a_\mu^{\mathrm{HLbL}}[\text{AV-tower+SDC}] = [20.6^{+1.3}_{-2.8}(4.7)(3.4)(0.3)_{\text{AV-poles}} + 4.2\,(0.1)_{\text{q-loop}(N_f=3)}] \times 10^{-11}, = 24.8\,(6.1) \times 10^{-11} \tag{34}$$

for the sum of both axial-vector tower and SDC contributions. Here, the first error in the result for the AV poles reflects the uncertainties in the matching scale $Q_{\min}$, whereas the second, third and fourth errors reflect uncertainties from the two-photon width, the uncertainties due to the mass scale and the variation of model parameters, similar as above. For the final result we average the first error and add the other errors in quadrature. Our final result is still in the ballpark of results from the holographic approach [50,51,55,56].

3.2 Light and heavy scalar mesons: $J^{PC} = 0^{++}$

The six representative scalar functions for the case of scalar meson exchange are given in Eq. (4.11) of Ref. [45], again with momenta $q_i^2 = -Q_i^2$ and their scalar transition form factors $\mathcal{F}_1^S, \mathcal{F}_2^S$ denoted in a basis which translates into ours according to

$$F_1^S = \mathcal{F}_1^S; \qquad F_2^S = -\mathcal{F}_2^S. \tag{35}$$

We start with the light scalar mesons. The $f_0(500)$ has been treated rigorously in the dispersive approach in terms of s-wave $\pi\pi$ rescattering, resulting in $a_\mu[f_0(500)] = -9\,(1) \times 10^{-11}$ [22,23]. This result has been confirmed later in Ref. [77]. In the same work, the rescattering contribution of the $f_0(980)$ has been estimated to result in $a_\mu[f_0(980)]$(rescattering) $= -0.2\,(1) \times 10^{-11}$. In the same reference, a corresponding quark model result in narrow width approximation (NWA) has been found to be $a_\mu[f_0(980)]$(NWA) $= -0.37\,(6) \times 10^{-11}$ using the normalisation condition

$$|F_1^S(0,0)|^2 = \frac{4\,\Gamma_{\gamma\gamma}}{\pi\alpha^2 m_S} \tag{36}$$

with $\Gamma_{\gamma\gamma}[f_0(980)] = 0.31\,(5)$ keV [79] for the TFFs. In order to make contact with their result, we adopt the same normalisation condition for our microscopically calculated TFFs. For the mass we use $m_{f_0(980)} = 990(20)$ MeV [79]. We then obtain

$$a_\mu^{\mathrm{HLbL}}[f_0(980)] = -0.287\,(46)\,(26)\,(4) \times 10^{-11}, \tag{37}$$

where the first error is due to the uncertainty in the decay width, the second one is by far dominated by the uncertainty in the experimental mass combined with the much smaller uncertainty due to the ambiguity in the mass factors of the matrix element (cf. corresponding explanations in the axialvector case), and the third one is our systematic model uncertainty as reflected in the error bands of the TFFs. Our result agrees with the rescattering result of Ref. [77] within error bars. In a similar spirit, for the $a_0(980)$ we also adopt the corresponding normalisation condition, this time with $\Gamma_{\gamma\gamma}[a_0(980)] = 0.5^{+0.2}_{-0.1}$ keV [81] and $m_{a_0(980)} = 980(20)$ MeV [79]:

$$a_\mu^{\mathrm{HLbL}}[a_0(980)] = -0.484\,(145)\,(45)\,(8) \times 10^{-11}, \tag{38}$$

where we averaged over the uncertainties in the decay width. Note that this uncertainty is much larger than the systematic uncertainty of our model. Within error bars, our result agrees with the (narrow width) quark model result of Ref. [77] and the very recent dispersive result $a_\mu^{\mathrm{HLbL}}[a_0(980)]_{\text{resc.}} = -0.43(1) \times 10^{-11}$ [82] taking into account re-scattering effects.

For the heavy meson multiplet above 1 GeV the experimental situation is worse. Following [77] we use again Eq. (36) with $\Gamma_{\gamma\gamma}[f_0(1370)] \leq 3.0^{+1.4}_{-0.9}$ keV and $\Gamma_{\gamma\gamma}[a_0(1450)] = 1.05^{+0.5}_{-0.3}$ keV [81]. The mass of the $f_0(1370)$ is not very well determined experimentally. We use again the Breit-Wigner mass $m_{f_0(1370)} = 1350(150)$ MeV [79] with extremely large error. The situation is much better for the a_0: $m_{a_0(1450)} = 1439(34)$ MeV. We then arrive at

$$a_\mu^{\mathrm{HLbL}}[f_0(1370)] = -0.673\,(258)\,(377)\,(7) \times 10^{-11}. \tag{39}$$

$$a_\mu^{\mathrm{HLbL}}[a_0(1450)] = -0.175\,(66)\,(22)\,(2) \times 10^{-11}. \tag{40}$$

where we averaged separately over the uncertainties in the decay width and the mass. These results are in the ballpark of the quark model narrow width estimate of Ref. [77].

4 Summary and conclusions

In this work we determined axial-vector and scalar meson exchange contributions to the HLbL tensor of a_μ. We worked within a microscopic approach to QCD using (a truncated set of) Dyson–Schwinger and Bethe–Salpeter equations, which have been successfully employed before to determine pseudoscalar exchange and box contributions to HLbL. From an effective underlying quark-gluon interaction we determined quark propagators, meson Bethe–Salpeter amplitudes, the quark-photon vertex and subsequently axial-vector and scalar transition form factors. We demonstrated explicitly that our approach preserves gauge invariance on a microscopic level and is therefore guaranteed to be free of artefacts stemming from otherwise non-zero extra tensor structures (cf. App. B). Our results for the scalar and axial-vector TFFs complement the ones for the pseudoscalar electromagnetic

Table 4 Results for various contributions to a_μ^{HLbL} in units of 10^{-11}. Compared are our results of Refs. [36,41] (pseudoscalar exchange and pseudoscalar boxes) and this work (axial-vector and scalar exchange) with the White Paper (WP) results of Ref. [4]

	DSE/BSE	WP
π exchange	62.6 (1)(1.3)	$63.0^{+2.7}_{-2.1}$
η exchange	15.8 (2)(3)(1.0)	16.3 (1.4)
η' exchange	13.3 (4)(3)(6)	14.5 (1.9)
π_0, η, η' exchange	91.6 (1.9)	$93.8^{+4.0}_{-3.6}$
π box	−15.7 (2)(3)	−15.9 (2)
K box	−0.48 (2)(4)	−0.46 (2)
π, K boxes/loops	−16.2 (5)	−16.4 (5)
s-wave $\pi\pi$ rescattering	not calc.	−8.0 (1.0)
higher scalar exchange	−1.6 (5)	−2.0 (2.0)
AV exchange (single)	17.4 (6.0)	6.0 (6.0)
AV exchange (tower) + SDC	24.8 (6.1)	21.0 (16.0)

and transition form factors determined in Refs. [36,41]. We provided explicit representations of these form factors that satisfy the large-momentum constraints. Our pseudoscalar and axial-vector TFFs agree with experimental information at zero momenta, see [36,41] and the discussion around Eq (14) in this work. For the scalar TFFs we used experimental information for the two-photon decay width as input to provide for a correct normalisation at zero momentum transfer. A further caveat concerns the short-distance constraints (SDCs) on the HLbL tensor itself. Although we took a tower of axial-vector contributions into account, we cannot show at present whether an infinite resummation of such a tower would satisfy these SDCs as it does in holographic QCD [50,51,55,56]. In contrast to their approach, our TFFs are given numerically, and much more refined numerical methods would be needed to extract the necessary information. This work is relegated to the future. Instead, we applied a matching procedure with the perturbative quark loop suggested in Refs. [29,54], which leads to a combined result of axial-vector and short-distance contributions.

Our collected results are given in Table 4 together with the corresponding results of the first White Paper [4]. We find very good agreement on all contributions within error bars. Our central result for the contributions from a single axial-vector multiplet is about a factor of three larger than the White Paper estimate, whereas the impact of SDCs turns out to be smaller than estimated for the White Paper. Taken together, however, the results overlap within error bars. To our mind, systematic cross-checks and comparisons between the dispersive approach, lattice QCD, holographic QCD and our approach to QCD via functional methods certainly has the potential to further decrease the spread of results and consequently the error bar of the axial-vector contributions to HLbL in the future.

Acknowledgements We are grateful to Igor Danilkin, Anton Rebhan and Peter Stoffer for discussions and to Anton Rebhan and Peter Stoffer for constructive comments on the manuscript. This work was supported by the Deutsche Forschungsgemeinschaft (DFG) under grant number Fi 970/11-2.

Data Availability Statement Data will be made available on reasonable request. [Authors' comment: The datasets generated during and/or analysed during the current study are available from the corresponding author on reasonable request.].

Code Availability Statement Code/software will be made available on reasonable request. [Authors' comment: The code/software generated during and/or analysed during the current study is available from the corresponding author on reasonable request.].

Appendix A: Axial-vector tensor basis

In this appendix we provide details on the construction of the axial-vector tensor basis in Eq. (6), see also Refs. [37,64,83,84]. The basis consists of four transverse tensors $\tau_{1\ldots4}^{\mu\nu\rho}$ which satisfy the constraints

$$Q^\mu \tau_i^{\mu\nu\rho} = 0, \qquad Q'^\nu \tau_i^{\mu\nu\rho} = 0. \tag{A1}$$

The remaining two non-transverse $\tau_{5,6}^{\mu\nu\rho}$ constitute the gauge part whose form factors must vanish. In addition, the transversality of the axial-vector meson also enforces transversality in the meson momentum. Equation (6) defines a 'minimal' basis in the sense that it is free of kinematic singularities and constraints, see e.g. Refs. [18,78,85–87]. Its derivation consists of four steps:

Step 1 is to write down the most general linearly independent tensor basis which shares the permutation-group symmetries of the full amplitude. In our case, these are the Bose symmetry constraints from Eq. (3), so all tensors should be Bose-symmetric as well. Furthermore, the basis should not contain any kinematic singularities and thus no divisions by the variables η_+, η_-, ω or combinations thereof. To this end, we start by writing down all possible expressions of the form $\tau^{\mu\nu\rho}(Q, Q')$ that can be constructed from the two momenta

Q and Q' and contain an epsilon tensor:

$$\begin{array}{ll} \varepsilon_Q^{\mu\nu\rho}, & \varepsilon_{QQ'}^{\mu\nu} \times \{Q^\rho,\ Q'^\rho\}, \\ \varepsilon_{Q'}^{\mu\nu\rho}, & \varepsilon_{QQ'}^{\mu\rho} \times \{Q^\nu,\ Q'^\nu\}, \\ & \varepsilon_{QQ'}^{\nu\rho} \times \{Q^\mu,\ Q'^\mu\}. \end{array} \tag{A2}$$

With the averaged four-momentum $\Sigma = (Q + Q')/2$, the Bose symmetry constraint (3) takes the form

$$\Lambda_A^{\mu\nu\rho}(\Sigma, \Delta) \stackrel{!}{=} \Lambda_A^{\nu\mu\rho}(-\Sigma, \Delta). \tag{A3}$$

We now construct linear combinations from Eq. (A2) that are either even or odd under this operation. Because the variable $\omega = \Sigma \cdot \Delta$ from Eq. (1) is also odd (whereas $\eta_\pm$ are even), we obtain even tensors if we attach a factor ω to the odd tensors:

$$\begin{aligned} K_1^{\mu\nu\rho} &= \varepsilon_{QQ'}^{\mu\nu} \Delta^\rho, \\ K_2^{\mu\nu\rho} &= \omega\, \varepsilon_{QQ'}^{\mu\nu} \Sigma^\rho, \\ K_3^{\mu\nu\rho} &= \varepsilon_\Sigma^{\mu\nu\rho}, \\ K_4^{\mu\nu\rho} &= \omega\, \varepsilon_\Delta^{\mu\nu\rho}, \\ K_5^{\mu\nu\rho} &= Q'^\mu \varepsilon_{QQ'}^{\nu\rho} + Q^\nu \varepsilon_{QQ'}^{\mu\rho}, \\ K_6^{\mu\nu\rho} &= \omega \left(Q'^\mu \varepsilon_{QQ'}^{\nu\rho} - Q^\nu \varepsilon_{QQ'}^{\mu\rho} \right), \\ K_7^{\mu\nu\rho} &= Q^\mu \varepsilon_{QQ'}^{\nu\rho} + Q'^\nu \varepsilon_{QQ'}^{\mu\rho}, \\ K_8^{\mu\nu\rho} &= \omega \left(Q^\mu \varepsilon_{QQ'}^{\nu\rho} - Q'^\nu \varepsilon_{QQ'}^{\mu\rho} \right). \end{aligned} \tag{A4}$$

It turns out that only six tensors are linearly independent, so we can drop K_7 and K_8:

$$\begin{aligned} K_7 &= -K_1 + 2\,(\eta_+ - \eta_-)\, K_3 - K_4 + K_5, \\ K_8 &= -2K_2 + 2\omega^2 K_3 - (\eta_+ + \eta_-)\, K_4 - K_6. \end{aligned} \tag{A5}$$

The amplitude can thus be written as

$$\Lambda_A^{\mu\nu\rho}(Q, Q') = \sum_{i=1}^{6} c_i(\eta_+, \omega)\, K_i^{\mu\nu\rho}(Q, Q'). \tag{A6}$$

Because all K_i are even and the amplitude itself is even, also the form factors $c_i(\eta_+, \omega)$ must be even and so they can only depend on ω^2.

Step 2 is to work out the gauge invariance constraints without introducing kinematic singularities, which is referred to as the Bardeen–Tung–Tarrach procedure [64,85,86]. Gauge invariance implies that the amplitude must be transverse in the photon legs, Eq. (4). The tensors K_1 and K_2 already satisfy both conditions individually. For the remaining ones we obtain

$$\begin{array}{ll} Q^\mu K_3^{\mu\nu\rho} = \frac{1}{2}\, \varepsilon_{QQ'}^{\nu\rho}, & Q'^\nu K_3^{\mu\nu\rho} = \frac{1}{2}\, \varepsilon_{QQ'}^{\mu\rho}, \\ Q^\mu K_4^{\mu\nu\rho} = -\omega\, \varepsilon_{QQ'}^{\nu\rho}, & Q'^\nu K_4^{\mu\nu\rho} = \omega\, \varepsilon_{QQ'}^{\mu\rho}, \\ Q^\mu K_5^{\mu\nu\rho} = \eta_-\, \varepsilon_{QQ'}^{\nu\rho}, & Q'^\nu K_5^{\mu\nu\rho} = \eta_-\, \varepsilon_{QQ'}^{\mu\rho}, \\ Q^\mu K_6^{\mu\nu\rho} = \omega\eta_-\, \varepsilon_{QQ'}^{\nu\rho}, & Q'^\nu K_6^{\mu\nu\rho} = -\omega\eta_-\, \varepsilon_{QQ'}^{\mu\rho}. \end{array} \tag{A7}$$

The transversality conditions then amount to

$$\begin{aligned} c_3 &= 2\,(\omega c_4 - \eta_-(c_5 + \omega c_6))\,, \\ c_3 &= -2\,(\omega c_4 + \eta_-(c_5 - \omega c_6))\,, \end{aligned} \tag{A8}$$

and taken together these result in

$$c_3 = -2\eta_- c_5, \qquad c_4 = \eta_- c_6. \tag{A9}$$

Plugging this back into Eq. (A6) yields

$$\Lambda_A^{\mu\nu\rho} = c_5\, X_1^{\mu\nu\rho} + c_6\, X_2^{\mu\nu\rho} + c_2\, X_3^{\mu\nu\rho} + c_1\, X_4^{\mu\nu\rho}, \tag{A10}$$

where the four $X_i^{\mu\nu\rho}$ are fully transverse and given by

$$\begin{aligned} X_1 &= K_5 - 2\eta_- K_3, \\ X_2 &= K_6 + \eta_- K_4, \\ X_3 &= K_2, \\ X_4 &= K_1. \end{aligned} \tag{A11}$$

The transversality of the two new tensors X_1 and X_2 can be made manifest by writing

$$\begin{aligned} X_1^{\mu\nu\rho} &= \varepsilon_Q^{\mu\rho\alpha}\, t_{QQ'}^{\alpha\nu} - t_{QQ'}^{\mu\alpha}\, \varepsilon_{Q'}^{\nu\rho\alpha}, \\ X_2^{\mu\nu\rho} &= -\omega \left(\varepsilon_Q^{\mu\rho\alpha}\, t_{QQ'}^{\alpha\nu} + t_{QQ'}^{\mu\alpha}\, \varepsilon_{Q'}^{\nu\rho\alpha} \right), \end{aligned} \tag{A12}$$

The tensors $X_1 \dots X_4$ carry mass dimensions 3, 5, 5, 3, respectively, so we may form the linear combinations

$$\begin{array}{ll} \tau_1 = \dfrac{X_1 - X_4}{2m_A^3}, & \tau_3 = \dfrac{2X_3}{m_A^5}, \\ \tau_2 = \dfrac{X_2 + 2X_3}{2m_A^5}, & \tau_4 = \dfrac{X_4}{m_A^3}. \end{array} \tag{A13}$$

These are the transverse tensors in Eq. (6).

Step 3: Gauge invariance is not always automatic, e.g. in the presence of a cutoff or, as demonstrated in Sect. B, in model calculations whose ingredients do not follow from a consistent truncation that preserves the vector Ward–Takahashi identity (WTI). Projecting such an amplitude onto the four tensors $\tau_{1\dots4}$ can induce kinematic singularities in the corresponding form factors. Thus one must complete the basis by adding those tensors that were eliminated in Eq. (A9), namely K_3 and K_4:

$$\tau_5 = \frac{K_3}{m_A}, \qquad \tau_6 = \frac{K_4}{m_A^3}. \tag{A14}$$

These constitute the gauge part. One thus arrives at a complete tensor basis consisting of a transverse part and a gauge part, whose associated form factors are now guaranteed to be free of kinematic singularities. For the scalar two-photon amplitude $\Lambda_S^{\mu\nu}$ the analogous procedure can be found in Sect II of Ref. [78]. Other examples are the quark-photon vertex [88], which consists of a transverse part and a Ball-Chiu part, where the latter satisfies a WTI, or nucleon Compton scattering and nucleon-to-resonance transition amplitudes [87].

Step 4: Because the onshell axial-vector meson is also transverse, technically we have another transversality condition

$$\Delta^\rho \Lambda_A^{\mu\nu\rho}(Q, Q') = 0 \tag{A15}$$

which can be worked out along the same lines. To this end, we start from Eq. (6) and keep only the first four tensors given that F_5^A and F_6^A vanish by gauge invariance. The contraction of Δ^ρ with the tensors τ_i in Eq. (6) yields

$$\begin{aligned}
\Delta^\rho \tau_1^{\mu\nu\rho} &= -\frac{\eta_+}{m_A^3}\,\varepsilon^{\mu\nu}_{QQ'},\\
\Delta^\rho \tau_2^{\mu\nu\rho} &= \frac{\omega^2}{m_A^5}\,\varepsilon^{\mu\nu}_{QQ'},\\
\Delta^\rho \tau_3^{\mu\nu\rho} &= \frac{2\omega^2}{m_A^5}\,\varepsilon^{\mu\nu}_{QQ'},\\
\Delta^\rho \tau_4^{\mu\nu\rho} &= \frac{\Delta^2}{m_A^3}\,\varepsilon^{\mu\nu}_{QQ'}.
\end{aligned} \tag{A16}$$

Unfortunately, the resulting constraint

$$\eta_+ F_1^A - \frac{\omega^2}{m_A^2}(F_2^A + 2F_3^A) - \Delta^2 F_4^A = 0, \tag{A17}$$

where $\Delta^2 = 2(\eta_+ - \eta_-)$, cannot be solved without introducing kinematic singularities. If we solve for F_4^A and plug the result back into Eq. (5), the resulting amplitude $(\Lambda_A^\perp)^{\mu\nu\rho}$ has a kinematic singularity at $\Delta^2 = 0$:

$$\begin{aligned}
(\Lambda_A^\perp)^{\mu\nu\rho} = m_A \Bigg[& F_1^A \left(\tau_1^{\mu\nu\rho} + \frac{\eta_+}{\Delta^2}\,\tau_4^{\mu\nu\rho}\right)\\
&+ F_2^A \left(\tau_2^{\mu\nu\rho} - \frac{\omega^2}{\Delta^2 m_A^2}\,\tau_4^{\mu\nu\rho}\right)\\
&+ F_3^A \left(\tau_3^{\mu\nu\rho} - \frac{2\omega^2}{\Delta^2 m_A^2}\,\tau_4^{\mu\nu\rho}\right)\Bigg].
\end{aligned} \tag{A18}$$

Because the onshell axial-vector meson amplitude is defined at $\Delta^2 = -m_A^2$, however, this is of no concern in practice because the limit $\Delta^2 = 0$ is never probed. Equation (A18) is just the transverse projection of the amplitude:

$$(\Lambda_A^\perp)^{\mu\nu\rho} = T_\Delta^{\rho\lambda} \sum_{i=1}^{3} F_i^A\, \tau_i^{\mu\nu\lambda}, \quad T^{\rho\lambda} = \delta^{\rho\lambda} - \frac{\Delta^\rho \Delta^\lambda}{\Delta^2}. \tag{A19}$$

Equation (A15) does therefore not provide any new information; it simply eliminates F_4^A while $F_{1,2,3}^A$ remain unchanged. In the microscopic expression (11), the origin of the transverse projector is the axial-vector meson amplitude. One may then equivalently evaluate Eq. (11) without that transverse projector, project on all six tensors and finally keep only the three physical form factors.

Appendix B: Comparison with model calculations

It is instructive to compare the results in Fig. 3 with model calculations of the axial-vector meson transition matrix element. To do so, we start with the simplest option, namely a tree-level quark-photon vertex $\Gamma^\mu = i\gamma^\mu$, a free quark propagator $S(k) = (-i\not{k}+m)/(k^2+m^2)$ with a constituent-quark mass m, and a monopole Bethe–Salpeter amplitude

$$\Gamma_A^\rho(k, \Delta) = \frac{\mathcal{C} m^2}{k^2 + m^2}\, i\gamma^\rho\gamma_5, \tag{B1}$$

where $\mathcal{C}$ is a strength parameter. The resulting form factors in the symmetric limit for $\mathcal{C} = 30$ and $m = 0.5$ GeV are shown in the leftmost panel of Fig. 6.

The two form factors F_5^A and F_6^A do not vanish, which signals that electromagnetic gauge invariance is broken. This may seem surprising given that the combination of a bare propagator and bare quark-photon vertex does satisfy the electromagnetic Ward–Takahashi identity (WTI)

$$Q^\mu \Gamma^\mu(k, Q) = S^{-1}(k + \tfrac{Q}{2}) - S^{-1}(k - \tfrac{Q}{2}). \tag{B2}$$

In fact, in this simple model the form factors can be calculated analytically using a Feynman parametrization. In the limit where all momenta vanish ($\omega = \eta_+ = \eta_- = 0$), and modulo colour and flavour traces, this yields

$$F_{1\ldots6}^A = \frac{\mathcal{C}}{(4\pi)^2}\left\{\frac{2\beta}{5},\ \frac{8\beta^2}{315},\ 0,\ -\frac{\beta}{3},\ \frac{4}{3},\ -\frac{\beta}{30}\right\} \tag{B3}$$

with $\beta = m_A^2/m^2$. In this approximation F_3^A vanishes identically for any momentum configuration. Moreover, the transversality of the axial-vector meson would eliminate F_4, but the remaining form factors F_5^A and F_6^A from the gauge part are still nonzero. Our calculation agrees with the analytic result in this limit, which serves as a useful check. Had we projected onto the first three tensors alone, the corresponding form factors would have picked up kinematic singularities.

Next, we exchange the model amplitude (B1) by the full amplitude calculated from its BSE (second panel in Fig. 6), see App. C for details. This does not improve the situation; the spurious form factor F_5^A is now even larger. In the third panel we implement the full propagator calculated from the quark DSE but keep the vertex bare, which violates the WTI. In the fourth panel we exchange the bare vertex by the Ball-Chiu vertex, which is the solution of the WTI (B2) for a general quark propagator. F_1^A is now much larger, F_2^A switched sign and became negative, and F_3^A is nonzero and positive. F_5^A and F_6^A are again sizeable even though the WTI holds.

Finally, the result including the full quark-photon vertex obtained from its BSE is shown in the fifth panel. The momentum falloff of all three form factors is now considerably steeper, F_2^A is large and positive and F_3^A small and negative. Most importantly, the gauge parts are now essentially zero. Their small remainders are presumably due to the fact

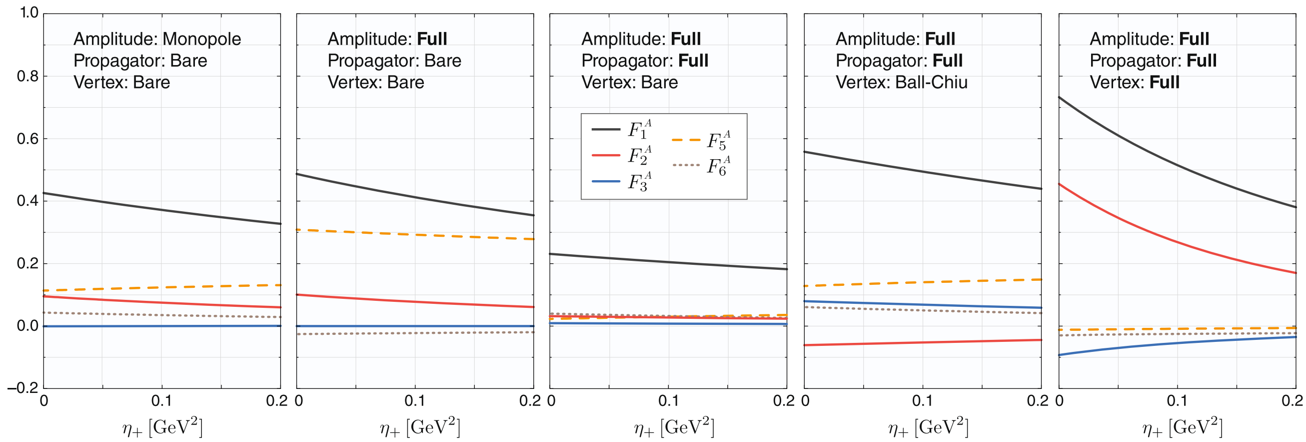

Fig. 6 Axial-vector transition form factors obtained from Eq. (11) using various model inputs. The rightmost panel corresponds to the full rainbow-ladder calculation (without the rescaling from Eq. (13))

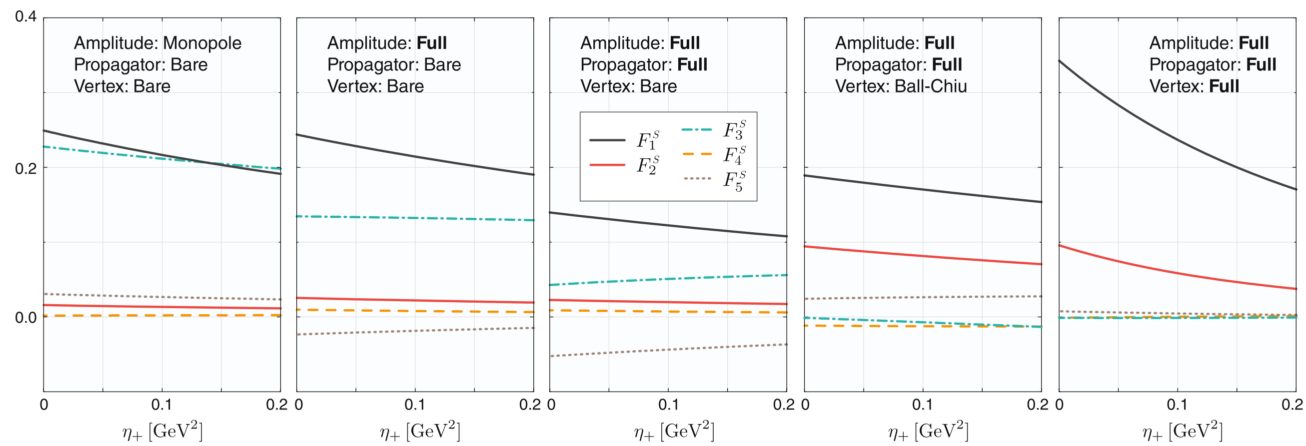

Fig. 7 Scalar transition form factors obtained from Eq. (11) using various model inputs analogous to Fig. 6

that we neglect the angular dependence of the quark-photon vertices in the form factor calculation to avoid problems with analytic continuations (which could be cured by solving the vertex BSE in a moving frame).

Figure 7 shows the same analysis for the scalar transition form factors using various model inputs. In the first panel we implement a bare propagator, a bare vertex, and a monopole amplitude

$$\Gamma_S(k,\Delta) = -\frac{\mathcal{C}m^2}{k^2+m^2}\,\gamma_5, \tag{B4}$$

again with $\mathcal{C} = 30$ and a constituent-quark mass $m = 0.5$ GeV. Clearly, the three form factors F_3^S, F_4^S and F_5^S from the gauge part are nonzero. This does not change when we exchange selected model ingredients with their calculated results (second to fourth panels). Only if all ingredients come from the consistent rainbow-ladder calculation, the unphysical form factors vanish (fifth panel).

It is interesting that the consistency between the quark propagator and quark-photon vertex through the WTI in Eq. (B2) is sufficient to ensure electromagnetic gauge invariance for electromagnetic form factors, where it boils down to charge conservation in the limit $Q^2 = 0$. For example, the neutron electromagnetic form factor automatically satisfies $G_E^n(Q^2 = 0) = 0$ if the WTI is satisfied, irrespective of the form of the baryon amplitude. By constrast, Figs. 6 and 7 show that for two-photon matrix elements electromagnetic gauge invariance operates at a deeper level, namely in the truncation of the DSEs and BSEs which simultaneously generate the quark propagator, quark-photon vertex and the meson amplitudes. The rainbow-ladder kernel ensures this because it satisfies both the vector and axial-vector WTIs. For calculations with model input, however, that link is broken.

Appendix C: Summary of technical elements

In the following we briefly outline the various steps needed to calculate the quark propagators, Bethe–Salpeter amplitudes and the quark-photon vertex needed to determine the axial-vector and scalar TFFs in the functional DSE approach. Details can be found in [41,59,65,67,69,89–91] and the review articles [63,92,93].

The necessary input to Eq. (11) is determined from a combination of DSEs and BSEs. The Bethe–Salpeter amplitude of a scalar/axial-vector meson and the quark-photon vertex satisfy (in-)homogeneous BSEs

$$[\Gamma_{\mathrm{M}}^{(\rho)}(p,P)]_{\alpha\beta} = \int_q [\mathbf{K}(p,q,P)]_{\alpha\gamma;\delta\beta} \times [S(q_+)\,\Gamma_{\mathrm{M}}^{(\rho)}(q,P)\,S(q_-)]_{\gamma\delta}, \tag{C1}$$

$$[\Gamma^{\mu}(p,P)]_{\alpha\beta} = Z_2\, i\gamma^{\mu}_{\alpha\beta} + \int_q [\mathbf{K}(p,q,P)]_{\alpha\gamma;\delta\beta} \times [S(q_+)\,\Gamma^{\mu}(q,P)\,S(q_-)]_{\gamma\delta}, \tag{C2}$$

where $\mathbf{K}$ is the Bethe–Salpeter kernel, Z_2 the quark renormalisation constant, and in both equations $q_\pm = q \pm P/2$. The quark propagator S is given by its DSE,

$$S^{-1}(p) = Z_2\,(i\not{p} + Z_m m_q) - Z_{1f}\, g^2\, C_F \int_q i\gamma^{\mu}\, S(q)\,\Gamma^{\nu}_{\mathrm{qg}}(q,p)\, D^{\mu\nu}(k), \tag{C3}$$

where m_q is the current-quark mass, $k = q - p$, $C_F = 4/3$, $D^{\mu\nu}$ is the dressed gluon propagator, $\Gamma^{\nu}_{\mathrm{qg}}$ the dressed quark-gluon vertex and Z_2, Z_m and Z_{1f} are renormalisation constants. The gluon propagator and quark-gluon vertex satisfy their own DSEs which include further n-point functions, so that in all practical applications the tower of DSEs needs to be truncated.

We work in Landau gauge and use the rainbow-ladder truncation, which together with more advanced schemes has been reviewed in Ref. [63]. To this end one defines an effective running coupling $\alpha(k^2)$ that incorporates dressing effects of the gluon propagator and the quark-gluon vertex. In the quark DSE this entails

$$Z_{1f}\, g^2\, \Gamma^{\nu}_{\mathrm{qg}}(q,p)\, D^{\mu\nu}(k) \;\to\; Z_2^2\, \frac{4\pi\alpha(k^2)}{k^2}\, T_k^{\mu\nu}\, i\gamma^{\nu} \tag{C4}$$

with transverse projector $T_k^{\mu\nu} = \delta^{\mu\nu} - k^{\mu}k^{\nu}/k^2$. The kernel $\mathbf{K}$ in the BSEs (C1–C2) is uniquely related to the quark-self energy by vector and axial-vector Ward–Takahashi identities. In rainbow-ladder truncation the kernel is given by

$$[\mathbf{K}(p,q,P)]_{\alpha\gamma;\delta\beta} \;\to\; Z_2^2\, \frac{4\pi\alpha(k^2)}{k^2}\, i\gamma^{\mu}_{\alpha\gamma}\, T_k^{\mu\nu}\, i\gamma^{\nu}_{\delta\beta}. \tag{C5}$$

This construction satisfies chiral constraints such as the Gell-Mann–Oakes–Renner relation and ensures the (pseudo-)Goldstone boson nature of the pion. Once we have specified the explicit shape of the effective interaction $\alpha(k^2)$, all elements of the calculation of the form factors follow and there is no room for any additional adjustments.

Similarly to our previous work on the pion TFF [59], the pseudoscalar pole contributions to HLbL [41] and the pseudoscalar box contributions to HLbL [36] we use the Maris-Tandy model for the effective coupling $\alpha(k^2)$, Eq. (10) of Ref. [94], with parameters $\Lambda = 0.74$ GeV and $\eta = 1.8 \pm 0.2$ (the parameters ω and D therein are related to the above via $\omega D = \Lambda^3$ and $\omega = \Lambda/\eta$). The scale Λ is fixed via experimental input; we use the pion decay constant for this purpose. The variation of η then changes the shape of the quark-gluon interaction at small momenta, cf. Fig. 3.13 in Ref. [63], and we use it as a rough estimate of the truncation error. We work in the isospin symmetric limit of equal up/down quark masses. With a current light quark mass of $m_q = 3.57$ MeV at a renormalisation point $\mu = 19$ GeV we obtain a pion mass and pion decay constant of $m_{\pi^0} = 135.0(2)$ MeV and $f_{\pi^0} = 92.4(2)$ MeV. With the strange-quark mass fixed at $m_s = 85$ MeV the resulting kaon mass is $m_K = 495.0(5)$ MeV.

Appendix D: Numerical results for TFFs and fits

In Fig. 8 we show exemplary results for our axialvector form factors $F_i^A(x,w)$ in symmetric and asymmetric kinematics on a linear scale (left diagram) and for symmetric kinematics on a logarithmic scale (right diagram). The variables x and w have been defined in Sect. 2.3:

$$x = \frac{\eta_+}{m_\rho^2} = \frac{Q^2 + Q'^2}{2m_\rho^2}, \quad w = \frac{\omega}{\eta_+} = \frac{Q^2 - Q'^2}{Q^2 + Q'^2}, \tag{D1}$$

where m_ρ is fixed scale, which is kept constant in the fitting procedure. The concrete value of m_ρ in the fits is arbitrary; its only purpose is to introduce the dimensionless variable x and dimensionless fit parameters in Tables 1 and 2. For simplicity we chose the experimental value $m_\rho = 0.77$ GeV. The numerical results and fits are indistinguishable by eye, thus underlining the high quality of the parametrizations. For the scalar TFFs the fit quality is similar.

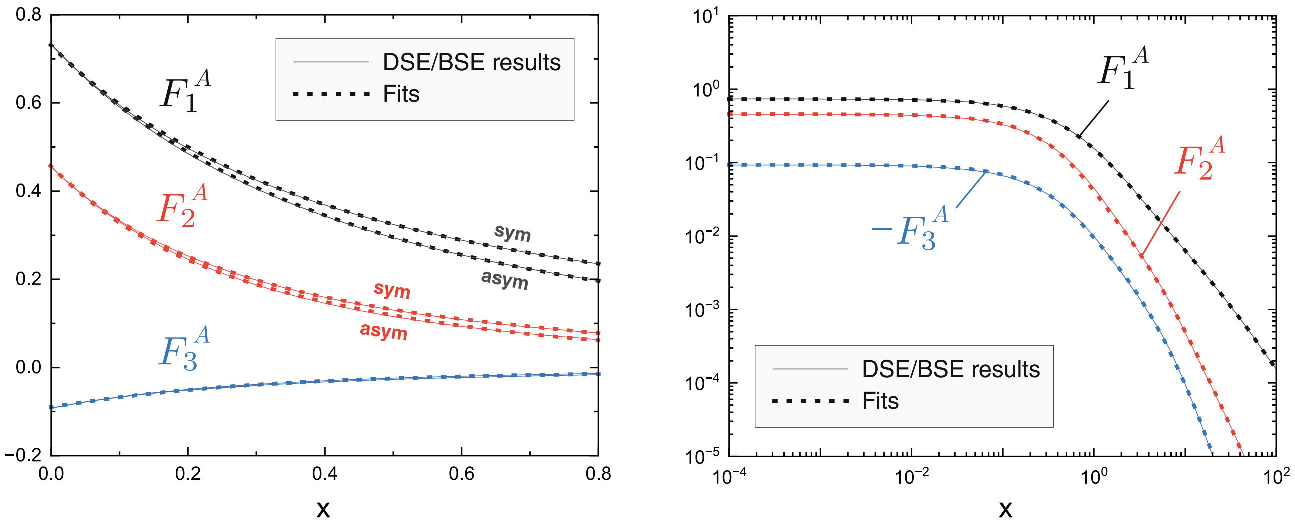

Fig. 8 Axial-vector transition form factors $F_i^A(x, w)$ obtained from our numerical calculation and compared with our fit functions, Eq. (20), without the rescaling from Eq. (13). The left diagram shows the TFFs both in the symmetric ($w = 0$) and asymmetric limit ($w = 1$) on a linear scale, whereas in the right diagram the TFFs in the symmetric limit are shown on a logarithmic scale

References

1. D.P. Aguillard et al. (Muon g-2), Phys. Rev. Lett. **131**, 161802 (2023). https://doi.org/10.1103/PhysRevLett.131.161802. arXiv:2308.06230 [hep-ex]
2. G.W. Bennett et al. (Muon g-2), Phys. Rev. **D73**, 072003 (2006). https://doi.org/10.1103/PhysRevD.73.072003. arXiv:hep-ex/0602035 [hep-ex]
3. B.L. Roberts, Chin. Phys. C **34**, 741 (2010). https://doi.org/10.1088/1674-1137/34/6/021. arXiv:1001.2898 [hep-ex]
4. T. Aoyama et al., Phys. Rep. **887**, 1 (2020). https://doi.org/10.1016/j.physrep.2020.07.006. arXiv:2006.04822 [hep-ph]
5. T. Aoyama, M. Hayakawa, T. Kinoshita, M. Nio, Phys. Rev. Lett. **109**, 111808 (2012). https://doi.org/10.1103/PhysRevLett.109.111808. arXiv:1205.5370 [hep-ph]
6. T. Aoyama, T. Kinoshita, M. Nio, Atoms **7**, 28 (2019). https://doi.org/10.3390/atoms7010028
7. A. Czarnecki, W.J. Marciano, A. Vainshtein, Phys. Rev. D **67**, 073006 (2003). https://doi.org/10.1103/PhysRevD.67.073006. arXiv:hep-ph/0212229. [Erratum: Phys. Rev. D 73, 119901 (2006)]
8. C. Gnendiger, D. Stöckinger, H. Stöckinger-Kim, Phys. Rev. D **88**, 053005 (2013). https://doi.org/10.1103/PhysRevD.88.053005. arXiv:1306.5546 [hep-ph]
9. M. Davier, A. Hoecker, B. Malaescu, Z. Zhang, Eur. Phys. J. C **77**, 827 (2017). https://doi.org/10.1140/epjc/s10052-017-5161-6. arXiv:1706.09436 [hep-ph]
10. A. Keshavarzi, D. Nomura, T. Teubner, Phys. Rev. D **97**, 114025 (2018). https://doi.org/10.1103/PhysRevD.97.114025. arXiv:1802.02995 [hep-ph]
11. G. Colangelo, M. Hoferichter, P. Stoffer, JHEP **02**, 006. https://doi.org/10.1007/JHEP02(2019)006. arXiv:1810.00007 [hep-ph]
12. M. Hoferichter, B.-L. Hoid, B. Kubis, JHEP **08**, 137. https://doi.org/10.1007/JHEP08(2019)137. arXiv:1907.01556 [hep-ph]
13. M. Davier, A. Hoecker, B. Malaescu, Z. Zhang, Eur. Phys. J. C **80**, 241 (2020). https://doi.org/10.1140/epjc/s10052-020-7792-2. arXiv:1908.00921 [hep-ph]. [Erratum: Eur. Phys. J. C 80, 410 (2020)]
14. A. Keshavarzi, D. Nomura, T. Teubner, Phys. Rev. D **101**, 014029 (2020). https://doi.org/10.1103/PhysRevD.101.014029. arXiv:1911.00367 [hep-ph]
15. B.-L. Hoid, M. Hoferichter, B. Kubis, Eur. Phys. J. C **80**, 988 (2020). https://doi.org/10.1140/epjc/s10052-020-08550-2. arXiv:2007.12696 [hep-ph]
16. A. Kurz, T. Liu, P. Marquard, M. Steinhauser, Phys. Lett. B **734**, 144 (2014). https://doi.org/10.1016/j.physletb.2014.05.043. arXiv:1403.6400 [hep-ph]
17. K. Melnikov, A. Vainshtein, Phys. Rev. D **70**, 113006 (2004). https://doi.org/10.1103/PhysRevD.70.113006. arXiv:hep-ph/0312226 [hep-ph]
18. G. Colangelo, M. Hoferichter, M. Procura, P. Stoffer, JHEP **09**, 091. https://doi.org/10.1007/JHEP09(2014)091. arXiv:1402.7081 [hep-ph]
19. G. Colangelo, M. Hoferichter, B. Kubis, M. Procura, P. Stoffer, Phys. Lett. B **738**, 6 (2014). https://doi.org/10.1016/j.physletb.2014.09.021. arXiv:1408.2517 [hep-ph]
20. G. Colangelo, M. Hoferichter, M. Procura, P. Stoffer, JHEP **09**, 074. https://doi.org/10.1007/JHEP09(2015)074. arXiv:1506.01386 [hep-ph]
21. P. Masjuan, P. Sanchez-Puertas, Phys. Rev. D **95**, 054026 (2017). https://doi.org/10.1103/PhysRevD.95.054026. arXiv:1701.05829 [hep-ph]
22. G. Colangelo, M. Hoferichter, M. Procura, P. Stoffer, Phys. Rev. Lett. **118**, 232001 (2017). https://doi.org/10.1103/PhysRevLett.118.232001. arXiv:1701.06554 [hep-ph]
23. G. Colangelo, M. Hoferichter, M. Procura, P. Stoffer, JHEP **04**, 161. https://doi.org/10.1007/JHEP04(2017)161. arXiv:1702.07347 [hep-ph]
24. M. Hoferichter, B.-L. Hoid, B. Kubis, S. Leupold, S.P. Schneider, Phys. Rev. Lett. **121**, 112002 (2018). https://doi.org/10.1103/PhysRevLett.121.112002. arXiv:1805.01471 [hep-ph]
25. M. Hoferichter, B.-L. Hoid, B. Kubis, S. Leupold, S.P. Schneider, JHEP **10**, 141. https://doi.org/10.1007/JHEP10(2018)141. arXiv:1808.04823 [hep-ph]

26. A. Gérardin, H.B. Meyer, A. Nyffeler, Phys. Rev. D **100**, 034520 (2019). https://doi.org/10.1103/PhysRevD.100.034520. arXiv:1903.09471 [hep-lat]
27. J. Bijnens, N. Hermansson-Truedsson, A. Rodríguez-Sánchez, Phys. Lett. B **798**, 134994 (2019). https://doi.org/10.1016/j.physletb.2019.134994. arXiv:1908.03331 [hep-ph]
28. G. Colangelo, F. Hagelstein, M. Hoferichter, L. Laub, P. Stoffer, Phys. Rev. D **101**, 051501 (2020). https://doi.org/10.1103/PhysRevD.101.051501. arXiv:1910.11881 [hep-ph]
29. G. Colangelo, F. Hagelstein, M. Hoferichter, L. Laub, P. Stoffer, JHEP **03**, 101. https://doi.org/10.1007/JHEP03(2020)101. arXiv:1910.13432 [hep-ph]
30. T. Blum, N. Christ, M. Hayakawa, T. Izubuchi, L. Jin, C. Jung, C. Lehner, Phys. Rev. Lett. **124**, 132002 (2020). https://doi.org/10.1103/PhysRevLett.124.132002. arXiv:1911.08123 [hep-lat]
31. G. Colangelo, M. Hoferichter, A. Nyffeler, M. Passera, P. Stoffer, Phys. Lett. B **735**, 90 (2014). https://doi.org/10.1016/j.physletb.2014.06.012. arXiv:1403.7512 [hep-ph]
32. V. Pauk, M. Vanderhaeghen, Eur. Phys. J. C **74**, 3008 (2014). https://doi.org/10.1140/epjc/s10052-014-3008-y. arXiv:1401.0832 [hep-ph]
33. I. Danilkin, M. Vanderhaeghen, Phys. Rev. D **95**, 014019 (2017). https://doi.org/10.1103/PhysRevD.95.014019. arXiv:1611.04646 [hep-ph]
34. F. Jegerlehner, *The Anomalous Magnetic Moment of the Muon*, vol. 274 (Springer, Cham, 2017). https://doi.org/10.1007/978-3-319-63577-4
35. M. Knecht, S. Narison, A. Rabemananjara, D. Rabetiarivony, Phys. Lett. B **787**, 111 (2018). https://doi.org/10.1016/j.physletb.2018.10.048. arXiv:1808.03848 [hep-ph]
36. G. Eichmann, C.S. Fischer, R. Williams, Phys. Rev. D **101**, 054015 (2020). https://doi.org/10.1103/PhysRevD.101.054015. arXiv:1910.06795 [hep-ph]
37. P. Roig, P. Sanchez-Puertas, Phys. Rev. D **101**, 074019 (2020). https://doi.org/10.1103/PhysRevD.101.074019. arXiv:1910.02881 [hep-ph]
38. M. Knecht, A. Nyffeler, Phys. Rev. D **65**, 073034 (2002). https://doi.org/10.1103/PhysRevD.65.073034. arXiv:hep-ph/0111058 [hep-ph]
39. A. Nyffeler, Phys. Rev. D **94**, 053006 (2016). https://doi.org/10.1103/PhysRevD.94.053006. arXiv:1602.03398 [hep-ph]
40. A. Gérardin, H.B. Meyer, A. Nyffeler, Phys. Rev. D **94**, 074507 (2016). https://doi.org/10.1103/PhysRevD.94.074507. arXiv:1607.08174 [hep-lat]
41. G. Eichmann, C.S. Fischer, E. Weil, R. Williams, Phys. Lett. B **797**, 134855 (2019). https://doi.org/10.1016/j.physletb.2019.134855. arXiv:1903.10844 [hep-ph]. [Erratum: Phys. Lett. B 799, 135029 (2019)]
42. K. Raya, A. Bashir, P. Roig, Phys. Rev. D **101**, 074021 (2020). https://doi.org/10.1103/PhysRevD.101.074021. arXiv:1910.05960 [hep-ph]
43. A. Gérardin, W.E.A. Verplanke, G. Wang, Z. Fodor, J.N. Guenther, L. Lellouch, K.K. Szabo, L. Varnhorst. (2023). arXiv:2305.04570 [hep-lat]
44. C. Alexandrou et al. (Extended Twisted Mass), Phys. Rev. D **108**, 094514 (2023). https://doi.org/10.1103/PhysRevD.108.094514. arXiv:2308.12458 [hep-lat]
45. M. Hoferichter, P. Stoffer, M. Zillinger, JHEP **04**, 092. https://doi.org/10.1007/JHEP04(2024)092. arXiv:2402.14060 [hep-ph]
46. J. Bijnens, N. Hermansson-Truedsson, L. Laub, A. Rodríguez-Sánchez, JHEP **10**, 203. https://doi.org/10.1007/JHEP10(2020)203. arXiv:2008.13487 [hep-ph]
47. J. Bijnens, N. Hermansson-Truedsson, L. Laub, A. Rodríguez-Sánchez, JHEP **04**, 240. https://doi.org/10.1007/JHEP04(2021)240. arXiv:2101.09169 [hep-ph]
48. J. Bijnens, N. Hermansson-Truedsson, A. Rodríguez-Sánchez, JHEP **02**, 167. https://doi.org/10.1007/JHEP02(2023)167. arXiv:2211.17183 [hep-ph]
49. K. Melnikov, A. Vainshtein. (2019). arXiv:1911.05874 [hep-ph]
50. J. Leutgeb, A. Rebhan, Phys. Rev. D **101**, 114015 (2020). https://doi.org/10.1103/PhysRevD.101.114015. arXiv:1912.01596 [hep-ph]
51. L. Cappiello, O. Catà, G. D'Ambrosio, D. Greynat, A. Iyer, Phys. Rev. D **102**, 016009 (2020). https://doi.org/10.1103/PhysRevD.102.016009. arXiv:1912.02779 [hep-ph]
52. P. Masjuan, P. Roig, P. Sanchez-Puertas, J. Phys. G **49**, 015002 (2022). https://doi.org/10.1088/1361-6471/ac3892. arXiv:2005.11761 [hep-ph]
53. J. Lüdtke, M. Procura, Eur. Phys. J. C **80**, 1108 (2020). https://doi.org/10.1140/epjc/s10052-020-08611-6. arXiv:2006.00007 [hep-ph]
54. G. Colangelo, F. Hagelstein, M. Hoferichter, L. Laub, P. Stoffer, Eur. Phys. J. C **81**, 702 (2021). https://doi.org/10.1140/epjc/s10052-021-09513-x. arXiv:2106.13222 [hep-ph]
55. J. Leutgeb, A. Rebhan, Phys. Rev. D **104**, 094017 (2021). https://doi.org/10.1103/PhysRevD.104.094017. arXiv:2108.12345 [hep-ph]
56. J. Leutgeb, J. Mager, A. Rebhan, Phys. Rev. D **107**, 054021 (2023). https://doi.org/10.1103/PhysRevD.107.054021. arXiv:2211.16562 [hep-ph]
57. M. Hoferichter, B. Kubis, M. Zanke, JHEP **08**, 209. https://doi.org/10.1007/JHEP08(2023)209. arXiv:2307.14413 [hep-ph]
58. J. Lüdtke, M. Procura, P. Stoffer. (2024). arXiv:2410.11946 [hep-ph]
59. G. Eichmann, C.S. Fischer, E. Weil, R. Williams, Phys. Lett. B **774**, 425 (2017). https://doi.org/10.1016/j.physletb.2017.10.002. arXiv:1704.05774 [hep-ph]
60. E. Weil, G. Eichmann, C.S. Fischer, R. Williams, Phys. Rev. D **96**, 014021 (2017). https://doi.org/10.1103/PhysRevD.96.014021. arXiv:1704.06046 [hep-ph]
61. T. Goecke, C.S. Fischer, R. Williams, Phys. Lett. B **704**, 211 (2011). https://doi.org/10.1016/j.physletb.2011.09.019. arXiv:1107.2588 [hep-ph]
62. D. Stamen, D. Hariharan, M. Hoferichter, B. Kubis, P. Stoffer, Eur. Phys. J. C **82**, 432 (2022). https://doi.org/10.1140/epjc/s10052-022-10348-3. arXiv:2202.11106 [hep-ph]
63. G. Eichmann, H. Sanchis-Alepuz, R. Williams, R. Alkofer, C.S. Fischer, Prog. Part. Nucl. Phys. **91**, 1 (2016). https://doi.org/10.1016/j.ppnp.2016.07.001. arXiv:1606.09602 [hep-ph]
64. M. Hoferichter, P. Stoffer, JHEP **05**, 159. https://doi.org/10.1007/JHEP05(2020)159. arXiv:2004.06127 [hep-ph]
65. P. Maris, P.C. Tandy, Phys. Rev. C **61**, 045202 (2000). https://doi.org/10.1007/JHEP05(2020)159. arXiv:nucl-th/9910033 [nucl-th]
66. P. Maris, P.C. Tandy, Nucl. Phys. A **663**, 401 (2000). https://doi.org/10.1016/S0375-9474(99)00627-2. arXiv:nucl-th/9908045 [nucl-th]
67. P. Maris, P.C. Tandy, Phys. Rev. C **65**, 045211 (2002). https://doi.org/10.1103/PhysRevC.65.045211. arXiv:nucl-th/0201017 [nucl-th]
68. M.S. Bhagwat, P. Maris, Phys. Rev. C **77**, 025203 (2008). https://doi.org/10.1103/PhysRevC.77.025203. arXiv:nucl-th/0612069 [nucl-th]
69. T. Goecke, C.S. Fischer, R. Williams, Phys. Rev. D **83**, 094006 (2011b). https://doi.org/10.1103/PhysRevD.83.094006. https://doi.org/10.1103/PhysRevD.86.099901. arXiv:1012.3886 [hep-ph]. [Erratum: Phys. Rev. D 86, 099901(2012)]
70. L. Chang, C.D. Roberts, Phys. Rev. C **85**, 052201 (2012). https://doi.org/10.1103/PhysRevC.85.052201. arXiv:1104.4821 [nucl-th]
71. R. Williams, C.S. Fischer, W. Heupel, Phys. Rev. D **93**, 034026 (2016). https://doi.org/10.1103/PhysRevD.93.034026. arXiv:1512.00455 [hep-ph]

72. W. Heupel, G. Eichmann, C.S. Fischer, Phys. Lett. B **718**, 545 (2012). https://doi.org/10.1016/j.physletb.2012.11.009. arXiv:1206.5129 [hep-ph]
73. N. Santowsky, G. Eichmann, C.S. Fischer, P.C. Wallbott, R. Williams, Phys. Rev. D **102**, 056014 (2020). https://doi.org/10.1103/PhysRevD.102.056014. arXiv:2007.06495 [hep-ph]
74. N. Santowsky, C.S. Fischer, Phys. Rev. D **105**, 034025 (2022). https://doi.org/10.1103/PhysRevD.105.034025. arXiv:2109.00755 [hep-ph]
75. M. Zanke, M. Hoferichter, B. Kubis, JHEP **07**, 106. https://doi.org/10.1007/JHEP07(2021)106. arXiv:2103.09829 [hep-ph]
76. P. Achard et al. (L3), Phys. Lett. B **526**, 269 (2002). https://doi.org/10.1016/S0370-2693(01)01477-0. arXiv:hep-ex/0110073
77. I. Danilkin, M. Hoferichter, P. Stoffer, Phys. Lett. B **820**, 136502 (2021). https://doi.org/10.1016/j.physletb.2021.136502. arXiv:2105.01666 [hep-ph]
78. G. Eichmann, C.S. Fischer, W. Heupel, Phys. Rev. D **92**, 056006 (2015). https://doi.org/10.1103/PhysRevD.92.056006. arXiv:1505.06336 [hep-ph]
79. S. Navas et al. (Particle Data Group), Phys. Rev. D **110**, 030001 (2024). https://doi.org/10.1103/PhysRevD.110.030001
80. P. Colangelo, F. Giannuzzi, S. Nicotri, Phys. Rev. D **109**, 094036 (2024). https://doi.org/10.1103/PhysRevD.109.094036. arXiv:2402.07579 [hep-ph]
81. J. Lu, B. Moussallam, Eur. Phys. J. C **80**, 436 (2020). https://doi.org/10.1140/epjc/s10052-020-7969-8. arXiv:2002.04441 [hep-ph]
82. O. Deineka, I. Danilkin, M. Vanderhaeghen. (2024). arXiv:2410.12894 [hep-ph]
83. J.H. Kuhn, J. Kaplan, E.G.O. Safiani, Nucl. Phys. B **157**, 125 (1979). https://doi.org/10.1016/0550-3213(79)90055-5
84. A.S. Rudenko, Phys. Rev. D **96**, 076004 (2017). https://doi.org/10.1103/PhysRevD.96.076004. arXiv:1707.00545 [hep-ph]
85. W.A. Bardeen, W.K. Tung, Phys. Rev. **173**, 1423 (1968). https://doi.org/10.1103/PhysRev.173.1423. [Erratum: Phys. Rev. D 4, 3229–3229 (1971)]
86. R. Tarrach, Nuovo Cim. A **28**, 409 (1975). https://doi.org/10.1007/BF02894857
87. G. Eichmann, G. Ramalho, Phys. Rev. D **98**, 093007 (2018). https://doi.org/10.1103/PhysRevD.98.093007. arXiv:1806.04579 [hep-ph]
88. J.S. Ball, T.-W. Chiu, Phys. Rev. D **22**, 2542 (1980). https://doi.org/10.1103/PhysRevD.22.2542
89. T. Goecke, C.S. Fischer, R. Williams, Phys. Rev. D **87**, 034013 (2013). https://doi.org/10.1103/PhysRevD.87.034013. arXiv:1210.1759 [hep-ph]
90. K. Raya, L. Chang, A. Bashir, J.J. Cobos-Martinez, L.X. Gutierrez-Guerrero, C.D. Roberts, P.C. Tandy, Phys. Rev. D **93**, 074017 (2016). https://doi.org/10.1103/PhysRevD.93.074017. arXiv:1510.02799 [nucl-th]
91. K. Raya, M. Ding, A. Bashir, L. Chang, C.D. Roberts, Phys. Rev. D **95**, 074014 (2017). https://doi.org/10.1103/PhysRevD.95.074014. arXiv:1610.06575 [nucl-th]
92. P. Maris, C.D. Roberts, Int. J. Mod. Phys. E **12**, 297 (2003). https://doi.org/10.1142/S0218301303001326. arXiv:nucl-th/0301049 [nucl-th]
93. P. Maris, P.C. Tandy, Proceedings, Cairns Topical Workshop on Light-Cone QCD and Nonperturbative Hadron Physics (Light Cone 2005). Nucl. Phys. Proc. Suppl. **161**, 136 (2006). https://doi.org/10.1016/j.nuclphysbps.2006.08.012. arXiv:nucl-th/0511017 [nucl-th]. [136 (2005)]
94. P. Maris, P.C. Tandy, Phys. Rev. C **60**, 055214 (1999). https://doi.org/10.1103/PhysRevC.60.055214. arXiv:nucl-th/9905056 [nucl-th]